

Planetary nebulae in the elliptical galaxy NGC 4649 (M 60): kinematics and distance redetermination¹

A. M. Teodorescu¹, R. H. Méndez¹, F. Bernardi², J. Thomas³, P. Das³, and O. Gerhard³

ana@ifh.hawaii.edu, mendez@ifh.hawaii.edu

ABSTRACT

Using a slitless spectroscopy method with (a) the 8.2 m Subaru telescope and its FOCAS Cassegrain spectrograph, and (b) the ESO Very Large Telescope (VLT) unit 1 (Antu) and its FORS2 Cassegrain spectrograph, we have detected 326 planetary nebulae (PNs) in the giant Virgo elliptical galaxy NGC 4649 (M 60), and we have measured their radial velocities. After rejecting some PNs more likely to belong to the companion galaxy NGC 4647, we have built a catalog with kinematic information for 298 PNs in M 60. Using these radial velocities we have investigated if they support the presence of a dark matter halo around M 60. The preliminary conclusion is that they do; based on an isotropic, two-component Hernquist model, we estimate the dark matter halo mass within $3R_e$ to be $4 \times 10^{11} M_\odot$, which is almost one half of the total mass of about $10^{12} M_\odot$ within $3R_e$. This total mass is similar to that estimated from globular cluster, XMM-Newton and Chandra observations. The dark matter becomes dominant outside. More detailed dynamical modeling of the PN data is being published in a companion paper. We have also measured the $m(5007)$ magnitudes of many of these PNs, and built a statistically complete sample of 218 PNs. The resulting PN luminosity function (PNLF) was used to estimate a distance modulus of 30.7 ± 0.2 mag, equivalent to 14 ± 1 Mpc. This confirms an earlier PNLf distance measurement, based on a much smaller sample. The PNLf distance modulus remains smaller than the surface brightness fluctuation (SBF) distance modulus by 0.4 mag. The reason is still unknown.

Subject headings: galaxies: distances and redshifts — galaxies: elliptical and lenticular, cD — galaxies: individual (NGC 4649) — galaxies: kinematics and dynamics — planetary nebulae: general — techniques: radial velocities

¹Institute for Astronomy, University of Hawaii, 2680 Woodlawn Drive, Honolulu, HI 96822

²Università di Pisa, Largo B. Pontecorvo 5, 56127, Pisa, Italy

³Max Planck Institut für Extraterrestrische Physik, P.O.Box 1603, D-85740 Garching bei München, Germany

1. INTRODUCTION

Planetary nebulae (PNs) in the outskirts of elliptical galaxies can be used as test particles to study dark matter existence and distribution (Hui et al. 1995; Méndez et al. 2001; Romanowsky et al. 2003; Teodorescu et al. 2005; De Lorenzi et al. 2008, 2009; Méndez et al. 2009; Coccato et al. 2009; Napolitano et al. 2010).

Sometimes the run of the line-of-sight velocity dispersion ($\text{LOS}V\sigma$) as a function of angular distance from the center of the galaxy shows clear evidence of dark matter; for example in NGC 5128 (Hui et al. 1995, Peng et al. 2004) or NGC 4374 (Napolitano et al. 2010). In other cases, the $\text{LOS}V\sigma$ shows a Keplerian decline with distance, indicating either the absence of a substantial dark matter halo, or the presence of significant radial anisotropy in the velocity distribution. Examples are NGC 4697 (Méndez et al. 2001, 2009; De Lorenzi et al. 2008) and NGC 3379 (De Lorenzi et al. 2009). It has been difficult to decide which interpretation (no dark matter or radial anisotropy) is to be preferred. The likelihood constraints from PNs seem to weakly prefer the dark matter plus anisotropy interpretation, but the uncertainties are large.

One strategy to further explore this problem could be to select an elliptical galaxy known to have a dark matter halo from other evidence; for example, the presence of hot, X-ray emitting gas. Do the PNs show a Keplerian decline of the $\text{LOS}V\sigma$ also in such a case? If yes, then radial anisotropy becomes the natural choice, and we have learned about an important constraint concerning the formation of ellipticals.

With this kind of outcome in mind, we selected the giant elliptical M 60 (NGC 4649) in the Virgo cluster. There is abundant X-ray emitting gas around this E2 galaxy (Fukazawa et al. 2006; Humphrey et al. 2006; Nagino & Matsushita 2009; Das et al. 2010). In addition, the globular cluster system of M 60 has been studied by Bridges et al. (2006), Hwang et al. (2008), and Shen & Gebhardt (2010). All these studies report the presence of a dark matter halo, as expected.

A few dozens of PNs were discovered in M 60 by Jacoby et al. (1990) as part of their effort to determine the distance to the Virgo cluster using the PN luminosity function (PNLF). To our knowledge their radial velocities were never measured.

In this paper we present the results of a search for PNs in several fields around M 60. Section 2 describes the observations, reduction procedures, PN detection and photometry.

¹Based partly on data collected at the Subaru Telescope, which is operated by the National Astronomical Observatory of Japan. Based partly on data collected at the European Southern Observatory, Chile, ESO Program 079.B-0577(A)

Section 3 deals with the slitless radial velocity method, its calibration and results. In Section 4 we present a catalog with all detected sources, and discuss which ones belong to the companion galaxy, the spiral NGC 4647. In section 5 we discuss rotation and the run of $\text{LOS}V\sigma$ as a function of angular distance from the center of M 60, make a first attempt to fit it using Hernquist models, and analyze a plot of the escape velocity as a function of angular distance. A more detailed dynamical analysis of M 60, based on the N-body made-to-measure code NMAGIC (De Lorenzi et al. 2007) is being published separately (Das et al. 2011). Section 6 is devoted to a redetermination of the distance to M 60 using the PNLf, and section 7 is a recapitulation.

2. OBSERVATIONS, REDUCTIONS, DETECTIONS, AND PHOTOMETRY

Planetary nebulae can be detected in the light of [O III] $\lambda 5007$ using the traditional on-band, off-band filter technique. Having taken the on-band image, insertion of a grism as dispersing element produces not only dispersion but also a displacement of all images. The dispersed images of PNs remain point sources, which permits an accurate measurement of the displacement. Calibration of the displacement as a function of wavelength and position in the CCD offers an efficient way of measuring radial velocities for all PNs in the field, irrespective of their number and distribution. We have described the method in several previous papers (Méndez et al. 2001, 2009; Teodorescu et al. 2005, 2010).

Because of the rather large angular size of M 60, with an effective radius $R_e = 128$ arcsec (Kormendy et al. 2009), we decided to observe several fields around M 60. Figure 1 shows the fields we observed, using the ESO Very Large Telescope (VLT) at the Cerro Paranal, Chile, and the Subaru telescope at Mauna Kea, Hawaii, USA. Chronologically, we first observed Field 1 in April 2007 with Subaru; because of poor seeing we reobserved Field 1, and added Field 2, in June 2007, with the VLT; finally, we reobserved Field 1 and added Field 3, in May 2008, with Subaru.

2.1. VLT Observations

Images and grism slitless spectra of M 60 were taken with the FORS2 spectrograph attached to the Cassegrain focus of unit telescope UT1 (Antu) of the ESO VLT, on the first halves of the nights of 2007 June 9/10 and 10/11. These half-nights were reasonably clear, but not of photometric quality, with thin cirrus clouds passing sometimes. The average seeing during these 2007 nights was 0.7 arcsec. FORS2, with the standard-resolution collimator,

gave a field of 6.8×6.8 arc minutes on a mosaic of two $2k \times 4k$ MIT CCD's (pixel size $15 \mu\text{m}$). All images were binned 2×2 . The image scale was $0.125 \text{ arcsec pixel}^{-1}$ before binning. The on-band and off-band interference filters had the following characteristics: effective central wavelengths, in observing conditions, of 5028 and 5300 Å; peak transmissions of 0.76 and 0.80; equivalent widths of 48.5 and 215 Å; and FWHMs of 60 and 250 Å. The dispersed images were obtained with the holographic grism 1400V. This grism gave a dispersion of 21 Å mm^{-1} , or $0.31 \text{ Å pixel}^{-1}$, at 5000 Å, before binning, and obviously $0.62 \text{ Å pixel}^{-1}$ after binning.

Table 1 lists the most important FORS2 science images obtained for this project, with the corresponding exposure times and air masses.

2.2. Subaru Observations

Images and grism slitless spectra of M 60 were taken with the Faint Object Camera and Spectrograph (FOCAS) attached to the Cassegrain focus of the 8.2 m Subaru telescope, Mauna Kea, Hawaii, on the nights of 2007 April 16 and 17, and of 2008 May 3 and 4. All these nights were of photometric quality, with the only exception of 2007 April 17, affected by some thin cirrus. The average seeing during the 2007 nights was one arcsec, and 0.6 arcsec in 2008.

FOCAS has been described by Kashikawa et al. (2002). The field of view of FOCAS is 6.5 arc minutes and was covered by two CCDs of $2k \times 4k$ (pixel size $15 \mu\text{m}$) with an unexposed gap of $5''$ between them. All images were binned 2×1 in the horizontal direction (perpendicular to dispersion) to increase the signal from the very faint sources we want to detect, but without compromising the spectral resolution. The image scale is $0.104 \text{ arcsec pixel}^{-1}$ after unbining. The on-band filter has a central wavelength of 5025 Å, a FWHM of 60 Å, a peak transmission of 0.68 and an equivalent width of 40 Å. Off-band imaging was done through the standard broadband visual filter. The dispersed images were obtained inserting an echelle grism with $175 \text{ grooves mm}^{-1}$ which operates in the 4th order and gives a dispersion of 0.5 Å pixel^{-1} , with an efficiency of 60%.

The spectrophotometric standard G 138-31 (Oke 1990) was used for the photometric calibration of the on-band images. Table 2 lists the most important FOCAS science images obtained for this project, with the corresponding exposure times and air masses.

2.3. Data reductions

Standard IRAF² tasks were used for the basic CCD reductions (bias subtraction, and flat field correction using twilight flats). In order to eliminate the cosmic-rays and to detect faint PN candidates, we needed to combine the scientific images of M 60 for each different field. The procedure we followed for this image combination has been carefully described in previous papers (e.g. Méndez et al. 2009, Teodorescu et al. 2010). For brevity, we do not repeat the description here.

For easier PN detection and photometry in the central parts of M60, where the background varies strongly across the field, we produced difference images between undispersed on-band and off-band combined frames. In ideal conditions, this image subtraction should produce a flat noise frame with the emission-line sources as the only visible features. A critical requirement to achieve the desired result is perfect matching of the point-spread functions (PSFs) of the two frames to be subtracted. For this purpose, we applied a method for “optimal image subtraction” developed by Alard & Lupton (1998), and implemented in Munich by Gössl & Riffeser (2002) as part of their image reduction pipeline.

This procedure cannot be used for the combined dispersed images, because there is no off-band counterpart. Therefore, to flatten the background and reduce the contamination by stellar spectra, we applied the IRAF task “fmedian” to the combined dispersed images. The resulting median images were then subtracted from the unmedianed ones.

2.4. PN detection and slitless spectroscopy

The PNs we want to find have strong [O III] $\lambda 5007$ emission and extremely weak, essentially absent continuum. We identified the PNs by blinking the on-band versus the off-band combined images, and confirmed them by blinking on-band versus dispersed. In addition, the object had to be a point source, and had to be undetectable in the off-band image. In this way it is possible to minimize the contamination of the PN sample by unrelated background sources, like galaxies with emission lines redshifted into the on-band filter transmission curve. We will further discuss contamination issues in Section 4. The (x and y) pixel coordinates of all the PN candidates in the undispersed and dispersed images were measured with the IRAF task “phot” with the centering algorithm “centroid”.

²IRAF is distributed by the National Optical Astronomical Observatories, operated by the Association of Universities for Research in Astronomy, Inc., under contract to the National Science Foundation

We performed an astrometric calibration of the images using the USNO-B1 astrometric star catalog (Monet et al. 2003), using a method we have described in Teodorescu et al. (2010). We estimate an rms of about 0.3 arcsec for the astrometry of our PNs.

2.5. Photometry

The purpose of our photometry was to obtain magnitudes $m(5007)$ as defined by Jacoby (1989):

$$m(5007) = -2.5 \log I(5007) - 13.74. \quad (1)$$

where $I(5007)$ is the [O III] 5007Å flux measured through the on-band filter. Since the FORS2 data were taken under non-photometric conditions, we restricted our photometric measurements to the FOCAS data, which were enough for our purposes (a redetermination of the PNLF distance). For the flux calibration, we adopted the spectrophotometric standard star G 138-31 (Oke 1990). This star has a monochromatic flux at 5025 Å of 1.51×10^{-15} erg cm⁻² s⁻¹ Å⁻¹ (Colina & Bohlin 1994). The flux measured through the on-band filter, in units of ergs cm⁻² s⁻¹, can be calculated knowing the equivalent width of the on-band filter; using equation (1), we find $m(5007)=19.31$ for G 138-31.

Many PNs were measurable only on the differences of the combined images (on – off). Thus, to calculate the $m(5007)$ of the PNs we had to go through several steps. First, we made aperture photometry of G 138-31 using the IRAF task “phot”. We also made aperture photometry of four moderately bright stars in the reference images selected for image registering. These four “internal standards” were selected relatively distant from the center of M 60, to avoid background problems.

Having tied the spectrophotometric standard to the internal frame standards, we switched to strictly differential photometry. We made aperture photometry of the internal standards on the on-band combined images to correct for any differences relative to the reference images. On the same on-band combined images we subsequently made PSF-fitting DAOPHOT photometry (Stetson 1987; IRAF tasks “phot”, “psf” and “allstar”) of the internal standards and four bright PNs. From the aperture photometry and PSF-fitting photometry of the internal standards we determined the aperture correction. Finally, we made PSF-fitting photometry of all PN candidates on the difference images (onband – offband), where the stars had been eliminated. The four bright PNs were used to tie this photometry to that of the standards. The internal errors in the photometry of the difference images were estimated to be below 5%. Applying a final correction related to the peak of the on-band filter transmission curve

(see Jacoby et al. 1987), we obtained $m(5007)$ for 272 PNs.

3. RADIAL VELOCITY CALIBRATIONS AND RESULTS

We have introduced changes in the calibration procedure required for the FORS2 data. Our original method (Méndez et al. 2001) used FORS1, where multiple slits could be defined using pairs of hanging blades. FORS2 allows to use especially designed masks covering the focal surface, making it possible to switch to a more convenient calibration method, which is the one that we used with FOCAS (Méndez et al. 2009). For brevity, we will limit our description to the FOCAS calibration.

In order to determine the shift produced by the insertion of the grism as a function of wavelength and position on the CCD, we used a special mask that produces an array of point sources when it is illuminated with the internal calibration lamps or any extended astronomical source. The full mask is made up of almost 1000 calibration points, separated by almost 100 pixels. We also used exposures of the local PN Abell 35 (NGC 303.6+40.0). This PN has a large angular size that allowed us to obtain calibration measurements all across the FOCAS field. An example of these calibration images is shown in Figure 2 of Méndez et al. (2009). The procedure for wavelength measurement is explained in Section 3 of that paper, to which we refer the interested reader.

For the wavelength calibration, after each grism exposure, the special mask was inserted in the light path, and on-band and grism + on-band images were obtained, illuminating the mask with the comparison lamp. In addition, on-band and grism + on-band images of the special mask were taken illuminating the mask with Abell 35, for radial velocity quality control.

To test for the presence of any systematic errors in the radial velocities, we use the images of Abell 35 as follows. We can measure radial velocities in two ways: (a) classical, using each mask hole as a slit, and (b) slitless, using the displacement introduced by the grism as a measure of wavelength, and therefore velocity. The comparison between slitless and classical measurement is shown in Figures 2 and 3 for Chip 1 and Chip 2, respectively. Since we are measuring the velocity of different gas elements in Abell 35, we expect to get a range of velocities across the field. There is good agreement between classical and slitless measurements, indicating no problems with the calibration of the slitless method. The average heliocentric velocity of Abell 35 from all the grid points is about -12 km s^{-1} , in good agreement with measurements of the systemic velocity ($-16 \pm 14 \text{ km s}^{-1}$, Jacoby 1981; $-7 \pm 4 \text{ km s}^{-1}$, Schneider et al. 1983). We conservatively estimate the calibration errors in

FOCAS slitless radial velocities to be of the order of 10 km s^{-1} . If we add quadratically the uncertainties in velocity given by the calibration errors ($\sim 10 \text{ km s}^{-1}$), the position errors ($\sim 10 \text{ km s}^{-1}$), and the errors from image registration ($\sim 10 \text{ km s}^{-1}$), we get an overall error of about 17 km s^{-1} . Assuming that the spectrograph deformations and guiding errors have a marginal contribution, we estimate the total uncertainty in the velocities measured with Subaru and FOCAS to be at most 20 km s^{-1} . The expected errors in FORS2 velocities are a bit larger, around 25 km s^{-1} , because of the slightly lower spectral resolution after binning. In Figure 4 we show a comparison of velocities for 50 objects that were measured with both spectrographs. We find a standard deviation of 40 km s^{-1} , which is not unreasonable, given the error bars reported for both instruments. Having found sufficiently good agreement, all available measurements for each object were averaged when building the catalog.

4. CATALOG OF PNs IN M 60

We have found 326 PN candidates in our search. Figure 5 shows them all. The x, y coordinates are measured in arcsec and are relative to the center of M 60. The x coordinate runs in the direction of increasing RA along the major axis of M 60, defined to be at P.A.= 105° (from N through E). The y coordinate runs in the direction of increasing Declination.

There is a complication introduced by the presence of the companion spiral galaxy NGC 4647. Some of our detections must belong to NGC 4647. Figure 6a is a histogram showing number of PNs as a function of velocity. There is a clear peak at the velocity of NGC 4697, which is 1409 km s^{-1} , according to the NASA/IPAC Extragalactic Database (NED). The peak is easily noticed mostly because the dispersion in radial velocity of this face-on spiral is very low.

In order to eliminate this source of contamination, we used a combination of two criteria (see McNeil et al. 2010). The first criterion is the relative surface brightness contribution from the two galaxies at the position of each PN. The surface brightness profile of M 60 was taken from Kuchinski et al. (2000) and Lee et al. (2008); that of NGC 4647 is from Kuchinski et al. The fit to M 60 was a $r^{1/4}$ profile, and the disk of NGC 4647 was fitted with an exponential law. The ratio of fluxes at the position of the PN was assumed to give the ratio of probability of membership based on light alone. The second and most important criterion is the relative likelihood that an object with a given velocity belongs to the velocity distribution of M 60 versus that of NGC 4647. The velocity distributions were approximated by Gaussians, and the probability of membership was calculated using the algorithm of Ashman et al. (1994). Since the NGC 4647 Gaussian is so narrow (100 km s^{-1}), this is the dominant factor. We have decided to reject 28 PNs that are less than

20 times more likely to belong to M 60 than to NGC 4647, according to the two combined criteria we have just described. Figure 6b shows the histogram for the remaining 298 objects; the NGC 4647 peak has disappeared.

Table 3 lists the 298 PNs we have accepted as belonging to M 60. Table 4 lists the 28 remaining PNs, which more probably (but not necessarily) belong to NGC 4647. Figure 7 shows the distribution of PNs near NGC 4647, indicating which ones were deleted from the M 60 list.

It may be useful to explain the naming strategy in Tables 3 and 4. Objects identified with an ID number < 300 appear in only one FOCAS field. If $600 < \text{ID} < 999$, the object has been detected in two FOCAS fields. If $1000 < \text{ID} < 1999$, the object is present in only one FORS2 field. If $2000 < \text{ID} < 2999$, the object is present in FORS2 Field1 Chip2, and Field2 Chip1. Objects seen with both FOCAS and FORS2 keep their FOCAS ID, unless no FOCAS velocity could be measured. In other words, objects having only a FORS2 velocity are identified with the FORS2 ID.

Figures 8 and 9 show the 298 M 60 PN velocities as functions of the x -coordinate in arcsec and the y -coordinate in arcsec, respectively. The average velocity of 1065 km s^{-1} is in reasonable agreement, within the uncertainties, with the NED radial velocity of 1117 km s^{-1} for M 60. We estimate the PN average velocity uncertainty to be approximately 30 km s^{-1} , from a velocity dispersion of the order of 300 km s^{-1} (see next section), the number of PNs measured, and the possible systematic error of $\pm 10 \text{ km s}^{-1}$ in our velocities from the calibration procedure using Abell 35. The 28 PNs we have assigned to NGC 4647 give an average velocity of 1447 km s^{-1} , again in reasonable agreement with the corresponding NED velocity of 1409 km s^{-1} for NGC 4647. But of course this was to be expected, because velocity was one of the two arguments we used to decide whether or not any given object could belong to NGC 4647.

In addition to PN sample contamination from NGC 4647, which we discussed above, we can also consider possible contamination by background galaxies having some emission line that has been redshifted into the on-band filter transmission curve. Given the spectral resolution of 0.5 \AA per pixel, the radial velocity resolution is about 140 km s^{-1} ; i.e., the PN internal velocity field is not resolved, and PNs appear as point sources. An emission line from a contaminating galaxy might be broader, but not necessarily so. Of course such a broad line would be immediately rejected as a PN, because it would not be a point source; therefore, we do not have that kind of contamination. But not all contaminating emission-line galaxies have necessarily broad lines; and so there could be contamination by narrow-emission galaxies. Knowing the central wavelength (5025 \AA) and the FWHM (60 \AA), it is easy to calculate, using the Doppler formula, the radial velocity range for detection of [O

III] $\lambda 5007$ (from -600 km s^{-1} to 2700 km s^{-1}). The observed radial velocity range is much narrower (from 200 to 1700 km s^{-1} , see Figures 8 and 9). Therefore, first, we are not missing any PNs; and second, contamination by background galaxies is not important, because such contaminants would be expected to be randomly distributed in wavelength across the filter transmission curve. Instead, we only find sources at the expected redshift of M 60, with the expected dispersion, and no discrepant velocities at all.

5. PRELIMINARY ANALYSIS OF M 60 RADIAL VELOCITIES

A deeper study of the kinematic information is deferred to another paper (Das et al. 2011). Here we limit ourselves to presenting a preliminary analysis, based on simple methods we have used previously to analyze other galaxies. Our main purpose is to study the run of the line-of-sight velocity dispersion ($\text{LOS}\sigma$). Since our measurement of the $\text{LOS}\sigma$ at large angular radii can be affected by rotation effects, we start by quantifying how important the rotation effects can be.

5.1. Rotation

We start with rotation along the major axis. Restricting our sample to those PNs with $|y| < 100 \text{ arcsec}$, we defined 5 groups with increasing average x coordinate, and calculated the average velocity for each group. The result is shown in Figure 10. We find that, on average, negative x objects are receding and positive x approaching, which is in agreement with the observed behavior of absorption-line data (Fisher et al. 1995, Pinkney et al. 2003) and globular clusters (Hwang et al. 2008). There is also some evidence of rotation in the perpendicular direction, i.e. along the minor axis. In Figure 9 we see two groups of PNs, with $y < -200$ and $y > 200$, respectively, with average velocities higher (1138 km s^{-1} ; 11 objects) and lower (974 km s^{-1} ; 25 objects) than the systemic velocity of M 60. This behavior is not observed in the globular cluster sample of Hwang et al. (2008), so its significance is not clear. We defer a discussion of rotation to the accompanying paper of Das et al. (2011). However, the existence of a velocity gradient as a function of the y coordinate will be taken into account when we discuss the behavior of the $\text{LOS}\sigma$.

5.2. Line-of-sight velocity dispersion

In order to study the $\text{LOS}V\sigma$, we subdivided our 298 PN sample into a central region and three elliptical annuli, with shapes similar to that of M 60, at increasing angular distances from the center of M 60. The numbers of PNs per region, from the inside out, are 75, 75, 74, and 74, respectively. The annuli are shown in Figure 11. For all PNs within each region we calculated the average angular distance to the center, and the $\text{LOS}V\sigma$. The result of these calculations is shown in Figure 12. The $\text{LOS}V\sigma$ derived from the PNs (four data points) is compared with that derived from major axis, long-slit, absorption-line spectra of M 60 (Fisher et al. 1995, Pinkney et al. 2003). We find reasonable agreement, within error bars, between PNs and absorption-line data within $60''$ of the galaxy’s center. We have added three more PN data points, obtained by isolating PNs with large positive y coordinates (25 objects), large negative y coordinates (11 objects), and large positive x coordinates (37 objects). The idea was to test if the differential motion of these groups around the center of M 60 can affect the measured $\text{LOS}V\sigma$. But the effect does not seem to be significant, with the only exception of the group with large positive x coordinates, which indeed gives a lower $\text{LOS}V\sigma$. Note that we do not have a similar number of PNs on the other side of the galaxy (large negative x coordinates) because of the presence of NGC 4647.

Let us consider what all this information tells us about dark matter existence and distribution in M 60. We start by making a rough estimate of the visible mass in this galaxy, from its blue luminosity and the $(M/L)_B$ ratio, which can be estimated from evolutionary population synthesis models. This has been done in the recent literature. If we follow, for example, Shen & Gebhardt (2010), using the tables and figures of Maraston (1998, 2005), we obtain an estimated $(M/L)_B = 10$ (this is based on a Salpeter initial mass function). Adopting a distance modulus of 31.1 mag (Blakeslee et al. 2009), an extinction-corrected $B_T = 9.7$, and the solar B absolute magnitude 5.47, we obtain for M 60 a blue luminosity of $6 \times 10^{10} L_\odot$, which then gives a mass of $6 \times 10^{11} M_\odot$.

We now ask if this visible mass is enough to explain the large central $\text{LOS}V\sigma$ in Figure 12. To investigate this, we use an analytical model by Hernquist (1990). This model is spherical, non-rotating, isotropic, and it assumes a constant mass-to-light ratio. We adopt an effective radius $R_e = 128''$ (Kormendy 2009), which is equivalent to 10.5 kpc for a distance of 17 Mpc, and a total mass of $6 \times 10^{11} M_\odot$. The fit (dotted line in Figure 12) obviously fails. In order to fit the central $\text{LOS}V\sigma$ we need a mass of $1.15 \times 10^{12} M_\odot$ (dashed line). But even this larger mass, assuming always a constant M/L ratio, cannot explain the large $\text{LOS}V\sigma$ at angular distances larger than 150 arcsec. A better fit can be obtained using a two-component Hernquist mass distribution, as in Hui et al. (1995):

$$M(r) = \frac{M_l r^2}{(r + a)^2} + \frac{M_d r^2}{(r + d)^2} \quad (2)$$

where M_l and M_d are the visible and dark matter total masses, and a and d are the corresponding scale lengths. Given the corresponding density and potential, we compute the projected velocity dispersion as a function of distance from the center using a code that numerically integrates the Jeans equation, assuming isotropic orbits, and expands the resulting three-dimensional and projected dispersions in Chebyshev polynomials. The two-component Hernquist model (solid line in Figure 12) successfully fits the observed $\text{LOS}\sigma$, if we adopt the following parameters: $M_l = 9.3 \times 10^{11} M_\odot$, $M_d = 6.6 \times 10^{12} M_\odot$, and $d = 17 a$ (note that in the Hernquist model, $R_e = 1.8153 a$). We do not attribute a lot of significance to the numerical values of these parameters; we are content with the implication that there seems to be a dark matter halo in the outskirts of M 60, as expected. However, for easier comparison with other studies in the literature, we will give a few specific numbers. From Eq. (2) we find that the dark matter halo mass within $3R_e$ is $4 \times 10^{11} M_\odot$, which is almost one half of the total mass of about $10^{12} M_\odot$ within $3R_e$. This total mass within $3R_e$ is similar to that estimated from XMM-Newton and Chandra observations; see, e.g., Figure 8 in Nagino & Matsushita (2009). The dark matter becomes dominant outside. The total mass within $3R_e$ derived by Shen & Gebhardt (2010) from globular cluster studies is a bit higher, namely a few times $10^{12} M_\odot$ (see their Figure 4).

Of course our use of Hernquist models is just a first approximation; in another paper (Das et al. 2011) we present a more careful dynamical analysis of M 60, based on the N-body made-to-measure code NMAGIC (De Lorenzi et al. 2007). Our purpose in the present paper is to make the PN database available, and make a first exploration of its significance.

In Figure 12 we find evidence suggesting that a significant fraction of the matter within a few R_e must be dark. This is in interesting contrast to the evidence in other galaxies like NGC 4697 and NGC 821 (Méndez et al. 2009, Teodorescu et al. 2010), where the one-component, constant mass-to-light ratio Hernquist model did provide a good fit to the run of the $\text{LOS}\sigma$ for a normal $(M/L)_B$ of 10 or less. Leaving that aside, the PN kinematics have passed the M 60 test; pending a more detailed study, we conclude in principle that, where independent evidence indicates the presence of an extended dark matter halo, the PNs give compatible results.

5.3. Escape velocities

We can make a complementary test, by plotting PN radial velocities as a function of angular distance from the center of M 60. Suppose we compare with the local escape velocity for the lower-mass Hernquist model with constant mass-to-light ratio used in Figure 12. The escape velocity is given by:

$$V_{\text{esc}} = (2GM_t/(r + a))^{0.5}, \quad (3)$$

where M_t is the total (stellar, visible) mass, and a is the scale length equal to $R_e/1.8153$. In the presence of a substantial dark matter contribution, we would expect some PNs to show velocities in excess of the escape velocity calculated from the visible mass, as shown in NGC 5128 by Hui et al. (1995) and Peng et al. (2004). Figure 13 shows that this is indeed the case in M 60. When we increase the mass to the level required to explain the $\text{LOS}\nu\sigma$, we no longer find unbound PNs.

6. THE PNLF, DISTANCE, AND PN FORMATION RATE

There is an unexplained discrepancy between PNLF distances and distances derived from the method of surface brightness fluctuations (SBF; Tonry et al. 2001). This problem has been described by Ciardullo et al. (2002), and a recent update is provided by Teodorescu et al. (2010). Since the original PNLF distance to M 60 (Jacoby et al. 1990) was based on a small sample of 17 PNs, in fact the smallest sample used in their paper, we decided it was worthwhile to make a PNLF distance redetermination using our much larger sample.

Having measured the apparent magnitudes $m(5007)$ of 272 PNs, we needed to produce a statistically complete sample, because the detectability of a PN varies with the background brightness. For this purpose we used a procedure that has been described in Section 5 of Méndez et al. (2001). In summary, we eliminated all PNs fainter than $m(5007) = 27.6$, beyond which the number of PNs per bin shows a marked decrease, indicating severe incompleteness; and we also eliminated all PNs within a zone of exclusion characterized by high background counts and more difficult detectability. This zone of exclusion was an ellipse at the center of M 60, with minor and major semiaxes of 40 and 50 arcsec, respectively. In this way, we got a statistically complete sample of 218 PNs.

The PN luminosity function (PNLF) was built, using 0.2 mag bins, and compared with simulated PNLFs like those used by Méndez & Soffner (1997) to fit the observed PNLF of M 31. The comparison is shown in Figure 14. The absolute magnitudes $M(5007)$ that produce

the best fit to the simulated PNLf were calculated using an extinction correction of 0.09 mag at 5007 Å (from data listed in the NED; see Schlegel et al. 1998) and a distance modulus $m - M = 30.7$, which is equivalent to a distance of 14 Mpc. The simulated PNLfs plotted in Figure 14 are binned, like the observed one, into 0.2 mag intervals, and have maximum final mass of $0.63 M_{\odot}$, $\mu_{\max} = 1$, and sample sizes between 2400 and 6700 PNs (see Méndez & Soffner 1997; the “sample size” is the total number of PNs, detected or not, that exist in the surveyed area). Since the observed PNLf shows an evident change of slope in Figure 14, the fit gives unambiguous information about both the distance modulus and the sample size. We estimate an error of 0.1 mag from the goodness of the fit at different distance moduli. To obtain the total error estimate, we have to combine the possible systematic and random errors. The systematic error is the same as in Jacoby et al. (1990), i.e., 0.13 mag, including the possible error in the distance to M 31, in the modeling of the PNLf and in the foreground extinction. The random contributions are given by 0.1 mag from the fit to the PNLf, 0.05 mag from the photometric zero point, and 0.05 mag from the filter calibration. Combining all these errors quadratically, we estimate that the total error bar for the PNLf distance modulus is ± 0.2 mag. The PNLf distance modulus, 30.7, is smaller than the SBF distance modulus (31.1, according to Tonry et al. 2001, and Blakeslee et al. 2009).

Our new PNLf distance is in excellent agreement with the previous PNLf distance estimate (Jacoby et al. 1990). Obviously, to obtain a reliable PNLf distance we do not need to observe so many PNs as we have done in this work. However, observing large samples opens the possibility of studying the *shape* of the PNLf in more detail than previously possible. Since we still lack a thorough understanding of the reason why the bright end of the PNLf is so insensitive to stellar population differences (e.g. Ciardullo 2006, Méndez et al. 2008), more empirical information about PNLf shapes could offer vital clues for progress.

One of the suggested ways of solving the PNLf-SBF discrepancy is by contamination of the PNLf with background galaxies that have some emission line redshifted into the on-band filter transmission curve. Teodorescu et al. (2010) have shown that this idea does not work; in several cases (NGC 1344, NGC 821, NGC 4697) we have the necessary amount of kinematic information to rule out a large number of contaminants. Since we have not found higher-redshift contaminants in M 60, we now have one more argument against the PNLf contamination idea.

Once we know the sample size (about 4000, from Figure 14), we can calculate the specific PN formation rate $\dot{\xi}$ in units of PNs $\text{yr}^{-1} L_{\odot}^{-1}$,

$$n_{\text{PN}} = \dot{\xi} L_{\text{T}} t_{\text{PN}}, \quad (4)$$

where n_{PN} is the sample size, L_{T} is the total bolometric luminosity of the sampled population, expressed in L_{\odot} , and t_{PN} is the lifetime of a PN, for which 30,000 yr was adopted in the PNLf simulations. Adopting an extinction-corrected $B_T = 9.7$, $B - V = 0.95$, a bolometric correction of -0.85 (Buzzoni et al. 2006), and a solar absolute bolometric magnitude 4.74, we obtain for M 60 a luminosity of $1.5 \times 10^{11} L_{\odot}$, of which we have sampled some $8 \times 10^{10} L_{\odot}$, if we discount the elliptical zone of exclusion at the center, and the area immediately near NGC 4647. Therefore, with $n_{\text{PN}} = 4000$, we obtain $\dot{\xi} = 1.7 \times 10^{-12}$ PNs $\text{yr}^{-1} L_{\odot}^{-1}$. We can also express the PN formation rate as $\alpha = n_{\text{PN}}/L_{\text{T}}$. Using that definition, we find $\log \alpha = -7.3$, in good agreement with the previous determination, as can be seen most easily in Figures 11 and 12 of Buzzoni et al. (2006).

The fact that we have found PNs associated with NGC 4647, with similar Jacoby magnitudes, tells us that its PNLf distance will be similar to that of M 60, as expected. We could have tried to obtain a more quantitative determination of the distance to NGC 4647 from the PNs in Table 4, but we have refrained from doing so, because the result would be unreliable. First of all, the number of objects is rather small. In addition, we might suffer extra uncertainty from extinction related to NGC 4647, which we cannot estimate. Finally, the NGC 4647 PNLf may be contaminated with a few M 60 PNs; some of the PNs that we have listed in Table 4 as “more likely to belong to NGC 4647” can conceivably belong instead to M 60, which is the dominant galaxy in this pair.

7. SUMMARY OF CONCLUSIONS

We have discovered many new PNs in M 60, and have built a catalog of 298 PNs with measured radial velocities. A preliminary study of the $\text{LOS}v_{\sigma}$ derived from this database indicates that some dark matter must be present within one R_{e} , and that there must be an extended dark matter halo, as expected from previous independent evidence. Thus, the kinematic information provided by the PNs proves to be qualitatively consistent, in principle, with inferences based on X-ray and globular cluster data. A more detailed dynamical study, using the N-body made-to-measure code NMAGIC (De Lorenzi et al. 2007), lies beyond the scope of this paper, and is being published separately (Das et al. 2011).

Photometry of most of the PNs has been used to build a statistically complete sample of 218 PNs. The resulting luminosity function has been used for a redetermination of the PNLf distance, finding excellent agreement with the earlier PNLf distance determination of Jacoby et al. (1990), which was based on a much smaller sample. The new PNLf distance modulus remains 0.4 mag smaller than the SBF distance modulus (Blakeslee et al. 2009).

This work was supported by the National Science Foundation (USA) under grants 0307489 and 0807522. In our research we made use of the NASA/IPAC Extragalactic Database (NED), which is operated by the Jet Propulsion Laboratory, California Institute of Technology, under contract with the National Aeronautics and Space Administration. It is a pleasure to acknowledge the help provided by the Subaru staff, in particular the support astronomer Takashi Hattori. Similar thanks are extended to the VLT staff at Cerro Paranal. We thank Jan Kleyna for making available a computer program required to compute the projected velocity dispersion as a function of distance from the center for a two-component Hernquist mass distribution. We thank the anonymous referee for some useful suggestions.

REFERENCES

- Alard, C., & Lupton, R.H. 1998, *ApJ*, 503, 325
- Ashman, K.M., Bird, C.M., & Zepf, S.E. 1994, *AJ*, 108, 2348
- Blakeslee, J.P., et al. 2009, *ApJ*, 694, 556
- Bridges, T., et al. 2006, *MNRAS*, 373, 157
- Buzzoni, A., Arnaboldi, M., & Corradi, R.L.M. 2006, *MNRAS*, 368, 877
- Ciardullo, R. 2006, in *IAU Symp. 234, Planetary Nebulae in our Galaxy and Beyond*, ed. M.J. Barlow & R.H. Méndez (Cambridge: Cambridge Univ. Press), 325
- Ciardullo, R., Feldmeier, J.J., Jacoby, G.H., Kuzio de Naray, R., Laychak, M.B., & Durrell, P.R. 2002, *ApJ*, 577, 31
- Coccato, L., et al. 2009, *MNRAS*, 394, 1249
- Colina, L., & Bohlin, R.C. 1994, *AJ*, 108, 1931
- Das, P., Gerhard, O., Churazov, E., & Zhuravleva, I. 2010, *MNRAS*, 409, 1362
- Das, P., Gerhard, O., Méndez, R.H., Teodorescu, A.M., & De Lorenzi, F. 2011, *MNRAS*, in press.
- De Lorenzi, F., Debattista, V.P., Gerhard, O., & Sambhus, N. 2007, *MNRAS*, 376, 71
- De Lorenzi, F., Gerhard, O., Saglia, R.P., Sambhus, N., Debattista, V.P., Pannella, M., & Méndez, R.H. 2008, *MNRAS*, 385, 1729

- De Lorenzi, F., et al. 2009, MNRAS, 395, 76
- Fisher, D., Illingworth, G., & Franx, M. 1995, ApJ, 438, 539
- Fukazawa, Y., Botoya-Nones, J.G., Pu, J., Ohto, A., & Kawano, N. 2006, ApJ, 636, 698
- Gössl, C.A., & Riffeser, A.. 2002, A&A, 381, 1095
- Hernquist, L. 1990, ApJ, 356, 359
- Hui, X., Ford, H.C., Freeman, K.C., & Dopita, M.A. 1995, ApJ, 449, 592
- Humphrey, P.J., Buote, D.A., Gastaldello, F., Zappacosta, L., Bullock, J.S., Brighenti, F., & Mathews, W.G. 2006, ApJ, 646, 899
- Hwang, H.S., et al. 2008, ApJ, 674, 869
- Jacoby, G.H. 1981, ApJ, 244, 903
- Jacoby, G.H. 1989, ApJ, 339, 39
- Jacoby, G.H., Ciardullo, R., & Ford, H.C. 1990, ApJ, 356, 332
- Jacoby, G.H., Quigley, R.J., & Africano, J.L. 1987, PASP, 99, 672
- Kashikawa, N., et al. 2002, PASJ, 54, 819
- Kormendy, J., Fisher, D.B., Cornell, M.E., & Bender, R. 2009, ApJS, 182, 216
- Kuchinski, L.E. et al. 2000, ApJS, 131, 441
- Lee, M.G., Park, H.S., Kim, E., Hwang, H.S., Kim, S.C., & Geisler, D. 2008, ApJ, 682, 135
- Maraston, C. 1998, MNRAS, 300, 872
- Maraston, C. 2005, MNRAS, 362, 799
- McNeil, E.K., Arnaboldi, M., Freeman, K.C., Gerhard, O.E., Coccato, L., & Das, P. 2010, A&A, 518, A44
- Méndez, R.H., Riffeser, A., Kudritzki, R.-P., Matthias, M., Freeman, K.C., Arnaboldi, M., Capaccioli, M., & Gerhard, O.E. 2001, ApJ, 563, 135
- Méndez, R.H. & Soffner, T. 1997, A&A, 321, 898
- Méndez, R.H., Teodorescu, A.M., Kudritzki, R.P., & Burkert, A. 2009, ApJ, 691, 228

- Méndez, R.H, Teodorescu, A.M., Schönberger, D., Jacob, R., & Steffen, M. 2008, *ApJ*, 681, 325
- Monet, D.J. et al. 2003, *ApJ*, 125, 984
- Nagino, R., & Matsushita, K. 2009, *A&A*, 501, 157
- Napolitano, N.R., et al. 2010, [arXiv:1010.1533v2](#)
- Oke, J.B. 1990, *AJ*, 99, 1621
- Peng, E.W., Ford, H.C., & Freeman, K.C. 2004, *ApJ*, 602, 685
- Pinkney, J. et al. 2003, *ApJ*, 596, 903
- Romanowsky, A.J., Douglas, N.G., Arnaboldi, M., Kuijken, K., Merrifield, M.R., Napolitano, N.R., Capaccioli, M., & Freeman, K.C. 2003, *Science*, 301, 1696
- Schlegel, D.J., Finkbeiner, D.P., & Davis, M. 1998, *ApJ*, 500, 525
- Schneider, S.E., Terzian, Y., Purgathofer, A., & Perinotto, M. 1983, *ApJS*, 52, 399
- Shen, J., & Gebhardt, K. 2010, *ApJ*, 711, 484
- Stetson, P.B. 1987, *PASP*, 99, 191
- Teodorescu, A.M., Méndez, R.H., Saglia, R.P., Riffeser, A., Kudritzki, R.-P., Gerhard, O.E., & Kleya, J. 2005, *ApJ*, 635, 290
- Teodorescu, A.M., Méndez, R.H., Bernardi, F., Riffeser, A., & Kudritzki, R.P. 2010, *ApJ*, 721, 369
- Tonry, J.L., Dressler, A., Blakeslee, J.P., Ahjar, E.A., Fletcher, A.B., Luppino, G.A., Metzger, M.R., & Moore, C.B. 2001, *ApJ*, 546, 681

Fig. 1.— Fields F1, F2, F3 observed for this project. The circular fields correspond to FOCAS, and the rectangular ones to FORS2. The spiral galaxy is NGC 4647. The total area of the sky shown here is 12.9×12.9 arc minutes.

Fig. 2.— Comparison of slitless vs slit (classical) radial velocities across Abell 35 for Chip 1 of FOCAS.

Fig. 3.— Comparison of slitless vs slit (classical) radial velocities across Abell 35 for Chip 2 of FOCAS.

Fig. 4.— Comparison of heliocentric slitless velocities measured with both FORS2 and FOCAS for 50 PN candidates. We plot FORS2 velocities (left) and (FOCAS – FORS2) velocities (right) as a function of FOCAS velocities. We obtain good agreement, with a standard deviation of 40 km s^{-1} .

Fig. 5.— Positions x, y in arc seconds, relative to the center of M 60, for the 326 PN candidates with measured velocities (plus signs). The square marks the position of the center of NGC 4647. The x coordinate runs in the direction of increasing RA, along the major axis of M 60. The y coordinate runs along the minor axis, in the direction of increasing Declination. Because of these choices, the sky appears flipped from left to right.

Fig. 6.— *Left*: Number of PNs as a function of velocity for 326 detections. There is a peak at the velocity of NGC 4647 (1409 km s^{-1}), indicating some contamination. *Right*: Number of PNs as a function of velocity for the 298 detections assigned to M 60 (see the text). The NGC 4647 peak has disappeared.

Fig. 7.— Positions x, y in arc seconds, relative to the center of M 60, for PNs near NGC 4647. The square indicates the center of NGC 4647. Objects rejected from the total sample, because they may belong to NGC 4647, are indicated with diamonds. Plus signs represent the M 60 PN sample.

Fig. 8.— Plus signs: heliocentric radial velocities of the 298 PNs as a function of their x -coordinates in arc seconds relative to the center of M 60. Diamonds: 28 objects listed in Table 4.

Fig. 9.— Plus signs: heliocentric radial velocities of the 298 PNs as a function of their y -coordinates in arc seconds relative to the center of M 60. Diamonds: 28 objects listed in Table 4.

Fig. 10.— Average velocities plotted as a function of average x coordinate for five PN groups, defined in the text. The numbers of objects in each group, from left to right, are 8, 42, 84,

35 and 24.

Fig. 11.— The elliptical annuli used to divide the plane of the sky into four regions, for the calculation of $\text{LOS}V\sigma$ s. Plus signs represent the 298 PNs in the M 60 sample.

Fig. 12.— $\text{LOS}V\sigma$ plotted as a function of average angular distance to the center of M 60. The PNs were divided into 4 regions, as explained in the text. These 4 data points are represented as squares. In addition, there is a diamond for PNs with large positive y , a triangle for PNs with large negative y , and an asterisk for PNs with large positive x . Plus signs are major axis, long-slit absorption-line data (Fisher et al. 1995, Pinkney et al. 2003). The dotted line represents the analytical model of Hernquist (1990), with a constant M/L ratio, a total mass of $6 \times 10^{11} M_{\odot}$, and $R_e = 128''$. The dashed line is the same kind of model, but with a higher mass of $1.15 \times 10^{12} M_{\odot}$. The solid line is a two-component Hernquist mass distribution, as described in the text.

Fig. 13.— Individual PN radial velocities plotted as a function of angular distance from the center of M 60. The solid lines are escape velocities for Hernquist models with total masses $1.2 \times 10^{12} M_{\odot}$ (outer lines) and $6 \times 10^{11} M_{\odot}$ (inner lines).

Fig. 14.— Observed [O III] $\lambda 5007$ PNLF of M 60 (squares), with the statistically complete sample of 218 PNs binned into 0.2 mag intervals. The apparent magnitudes $m(5007)$ have been transformed into absolute magnitudes $M(5007)$ by adopting an extinction correction of 0.09 mag and a distance modulus $m - M = 30.7$. The four lines are PNLf simulations (Méndez and Soffner 1997) for four different total PN population sizes: 2400, 3400, 4700, and 6700 PNs. We estimate the best-fit sample size to be 4000. From this sample size it is possible to estimate the PN formation rate (see the text).

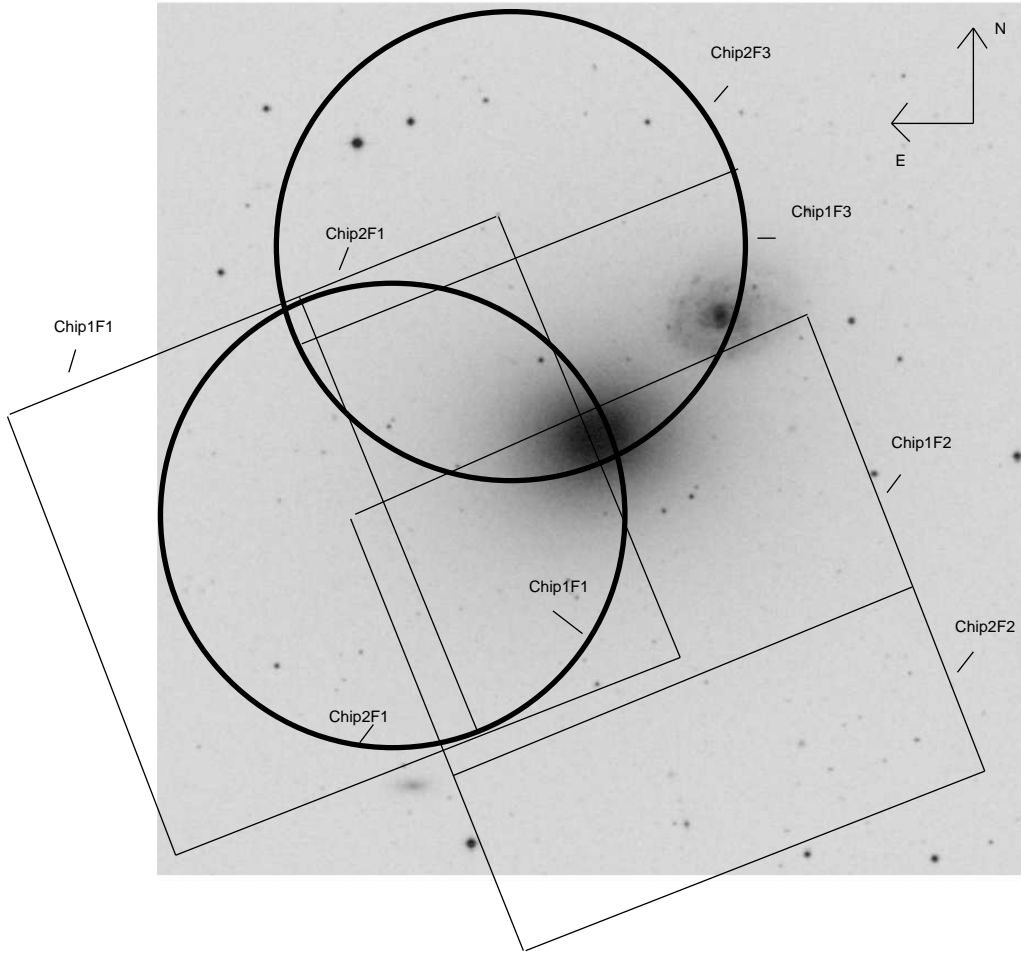


Fig. 1.— Fields F1, F2, F3 observed for this project. The circular fields correspond to FOCAS, and the rectangular ones to FORS2. The spiral galaxy is NGC 4647. The total area of the sky shown here is 12.9×12.9 arc minutes.

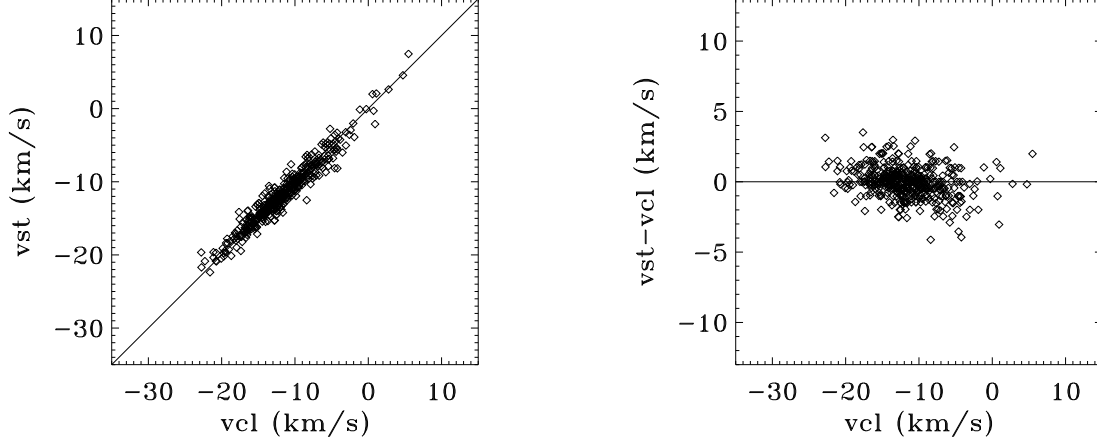


Fig. 2.— Comparison of slitless vs slit (classical) radial velocities across Abell 35 for Chip 1 of FOCAS.

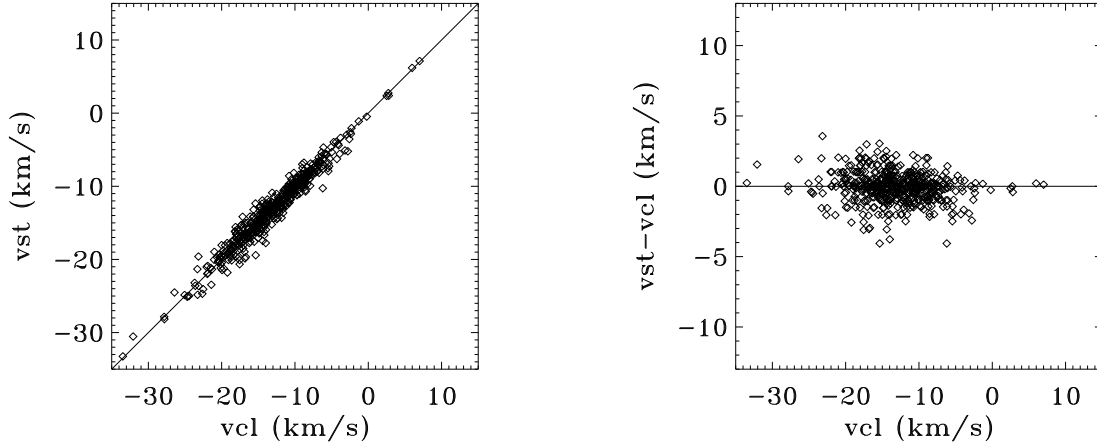


Fig. 3.— Comparison of slitless vs slit (classical) radial velocities across Abell 35 for Chip 2 of FOCAS.

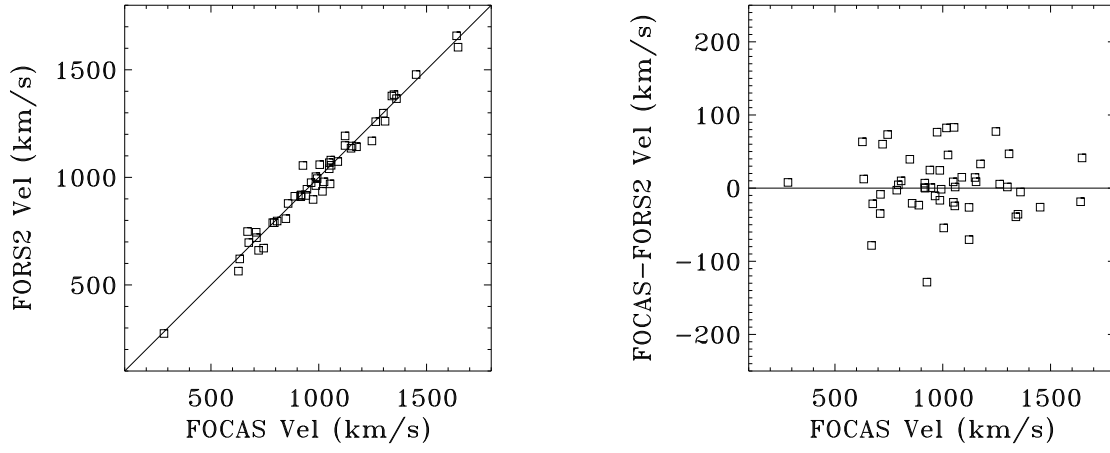


Fig. 4.— Comparison of heliocentric slitless velocities measured with both FORS2 and FOCAS for 50 PN candidates. We plot FORS2 velocities (left) and (FOCAS – FORS2) velocities (right) as a function of FOCAS velocities. We obtain good agreement, with a standard deviation of 40 km s^{-1} .

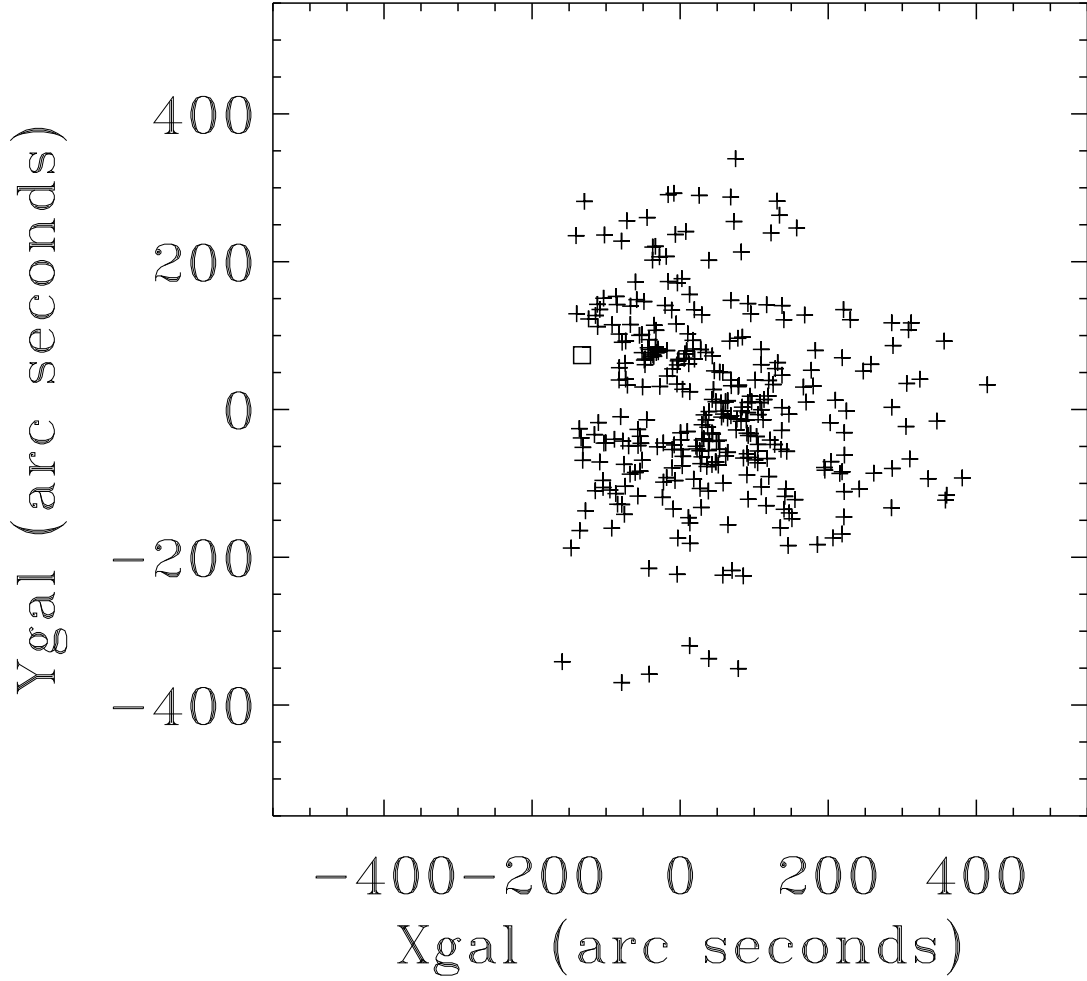


Fig. 5.— Positions x, y in arc seconds, relative to the center of M 60, for the 326 PN candidates with measured velocities (plus signs). The square marks the position of the center of NGC 4647. The x coordinate runs in the direction of increasing RA, along the major axis of M 60. The y coordinate runs along the minor axis, in the direction of increasing Declination. Because of these choices, the sky appears flipped from left to right.

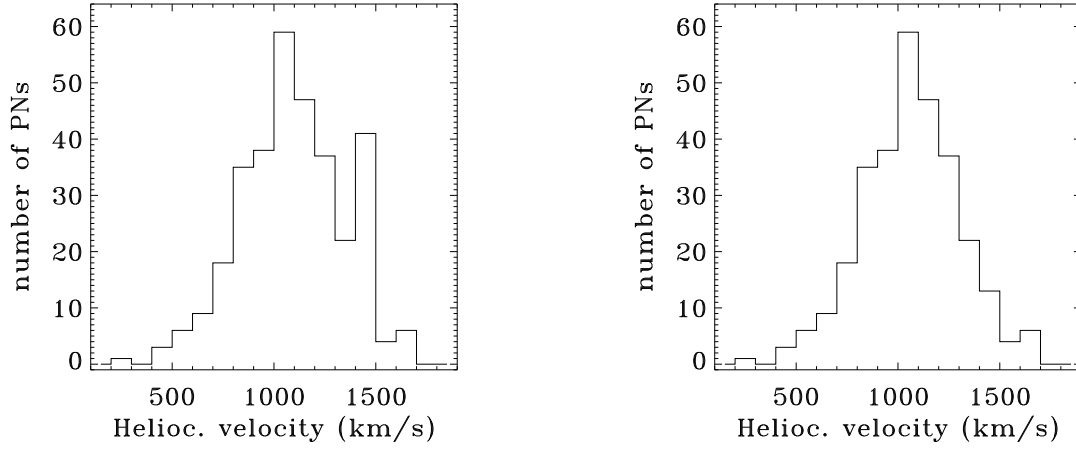


Fig. 6.— *Left*: Number of PNs as a function of velocity for 326 detections. There is a peak at the velocity of NGC 4647 (1409 km s^{-1}), indicating some contamination. *Right*: Number of PNs as a function of velocity for the 298 detections assigned to M 60 (see the text). The NGC 4647 peak has disappeared.

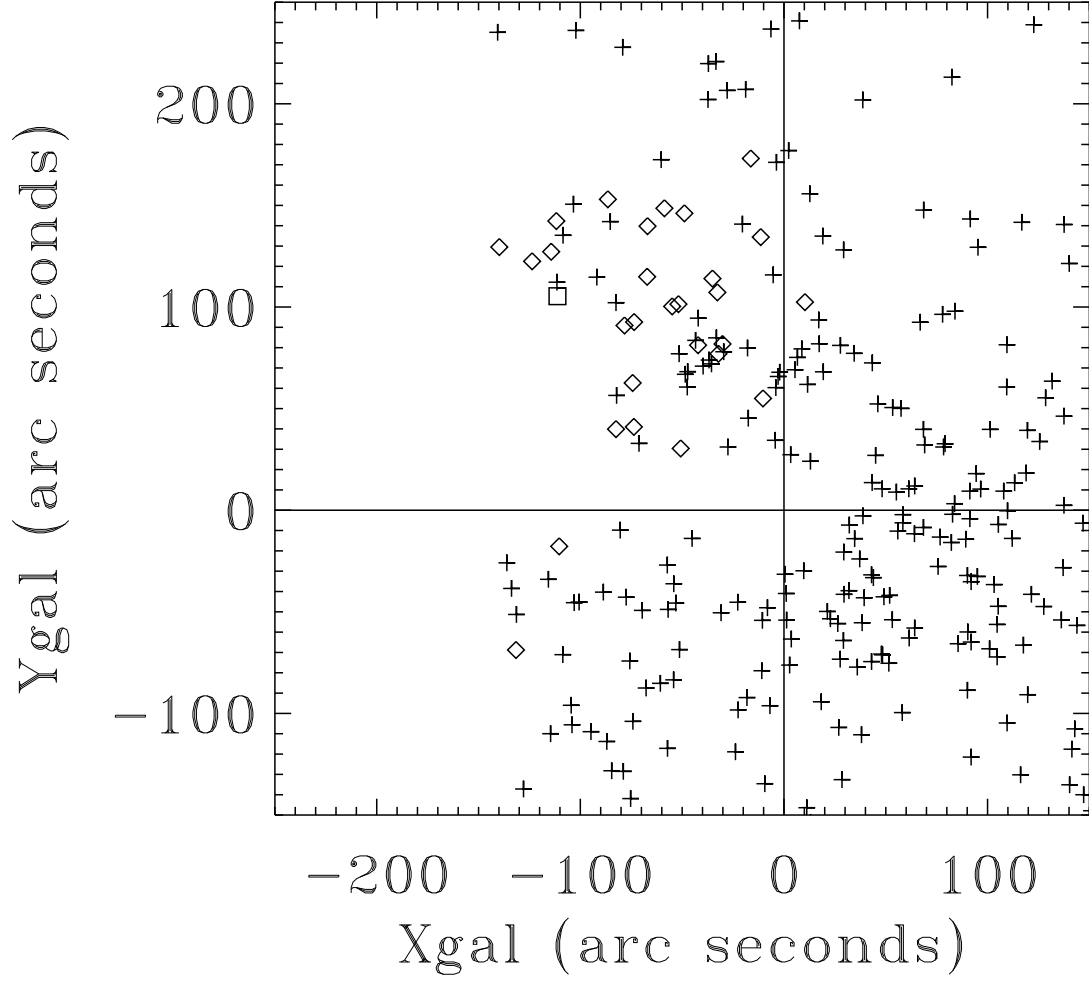


Fig. 7.— Positions x, y in arc seconds, relative to the center of M 60, for PNs near NGC 4647. The square indicates the center of NGC 4647. Objects rejected from the total sample, because they may belong to NGC 4647, are indicated with diamonds. Plus signs represent the M 60 PN sample.

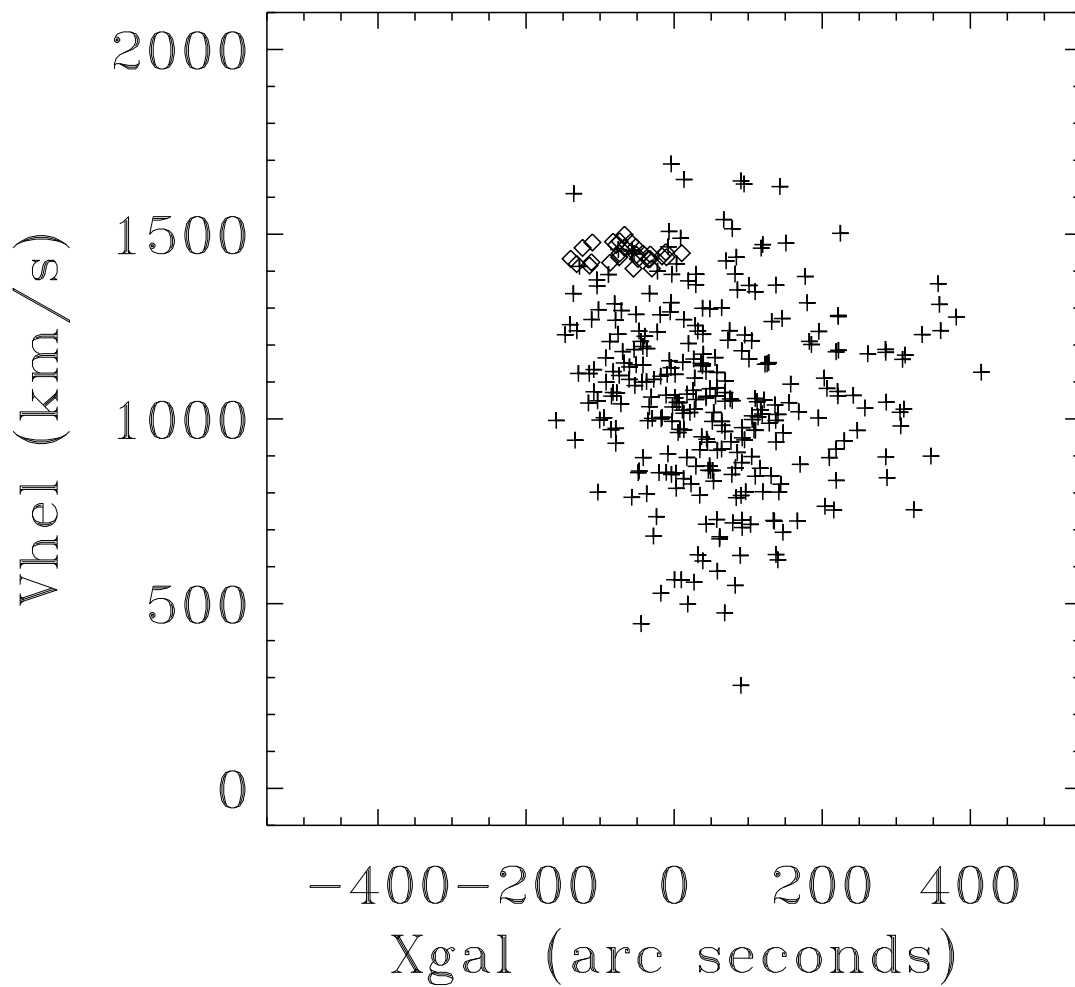


Fig. 8.— Plus signs: heliocentric radial velocities of the 298 PNs as a function of their x -coordinates in arc seconds relative to the center of M 60. Diamonds: 28 objects listed in Table 4.

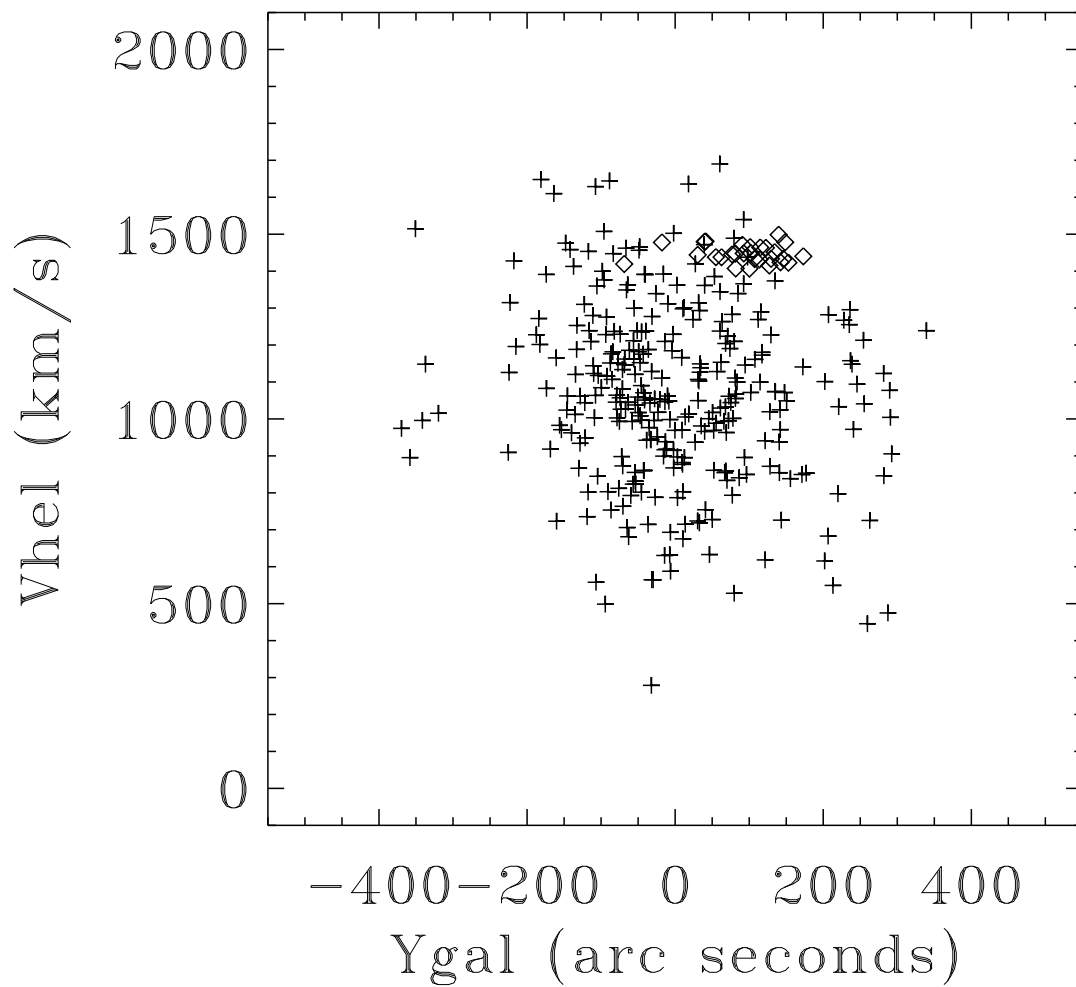


Fig. 9.— Plus signs: heliocentric radial velocities of the 298 PNs as a function of their y -coordinates in arc seconds relative to the center of M 60. Diamonds: 28 objects listed in Table 4.

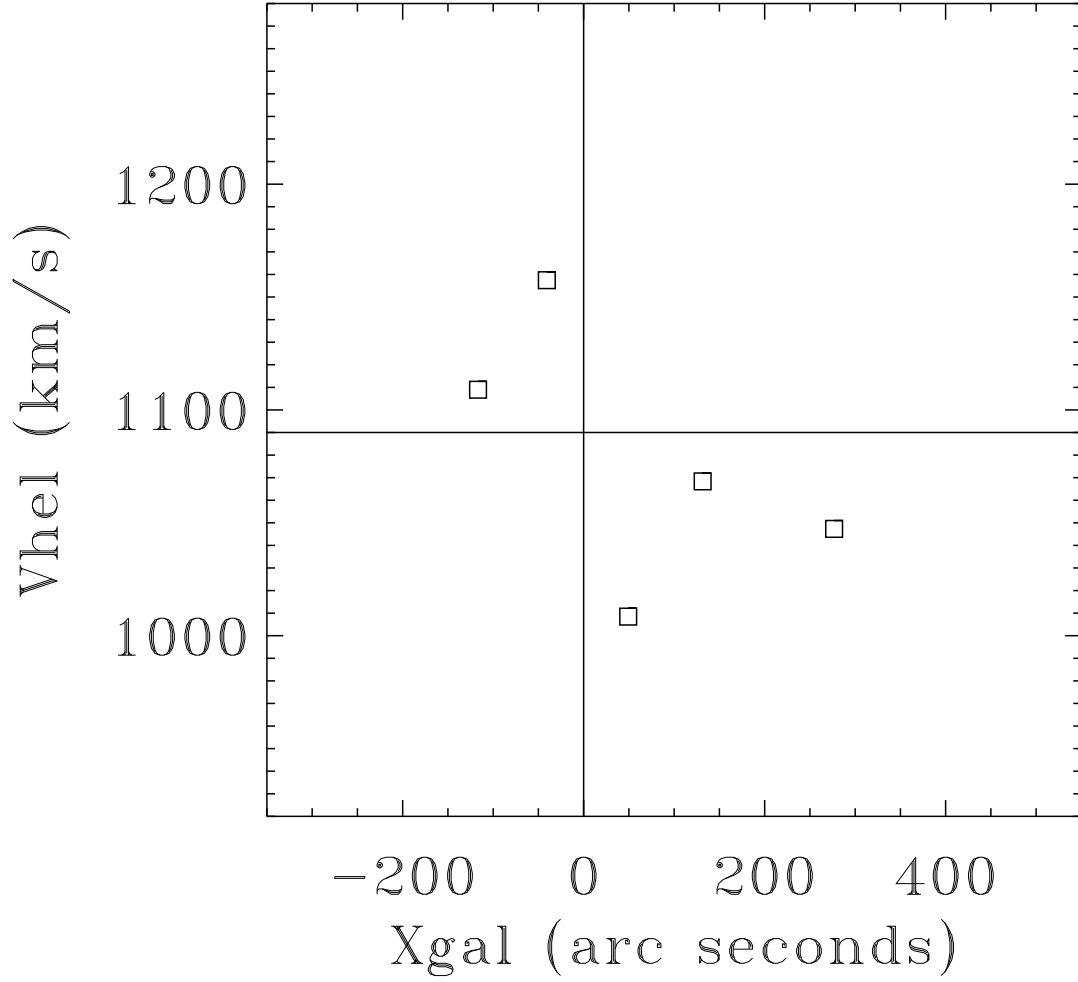


Fig. 10.— Average velocities plotted as a function of average x coordinate for five PN groups, defined in the text. The numbers of objects in each group, from left to right, are 8, 42, 84, 35 and 24.

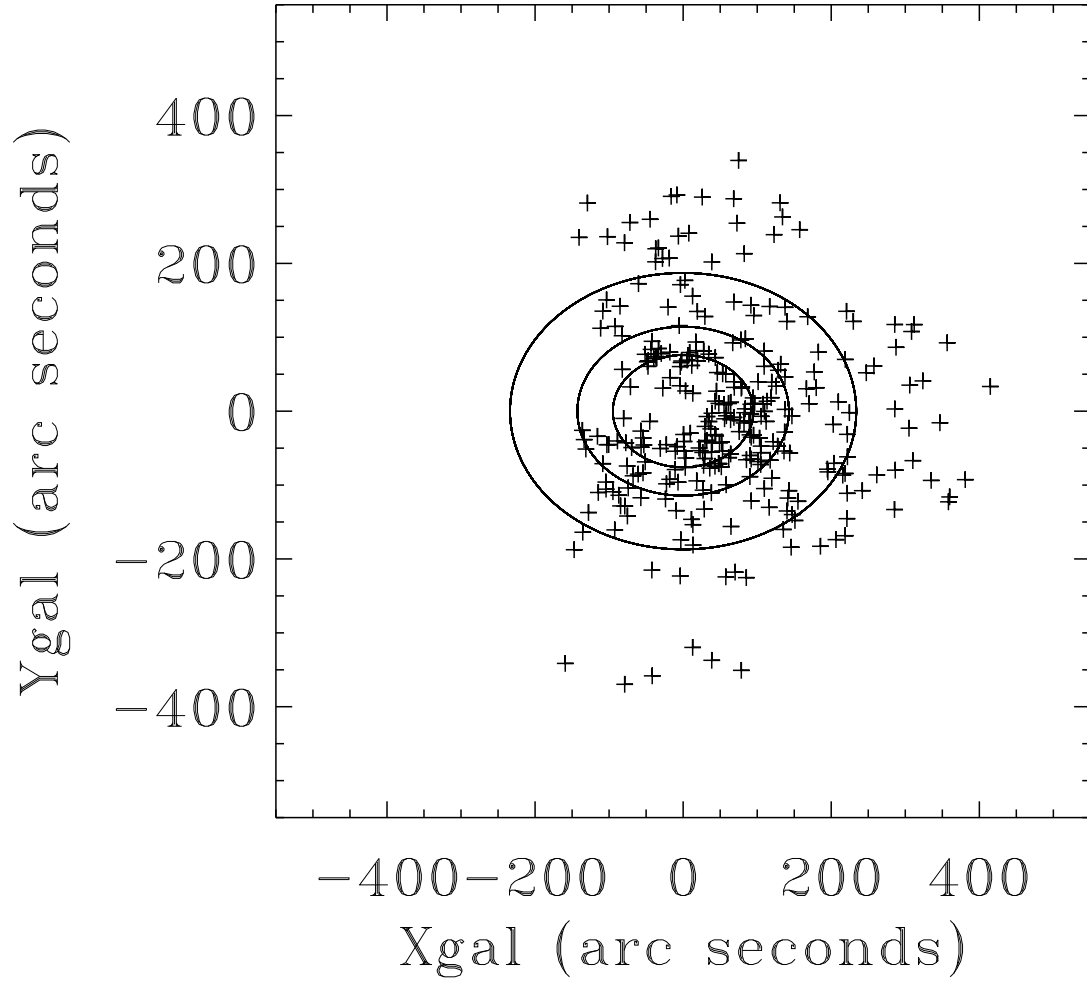


Fig. 11.— The elliptical annuli used to divide the plane of the sky into four regions, for the calculation of $\text{LOS}V\sigma$ s. Plus signs represent the 298 PNs in the M 60 sample.

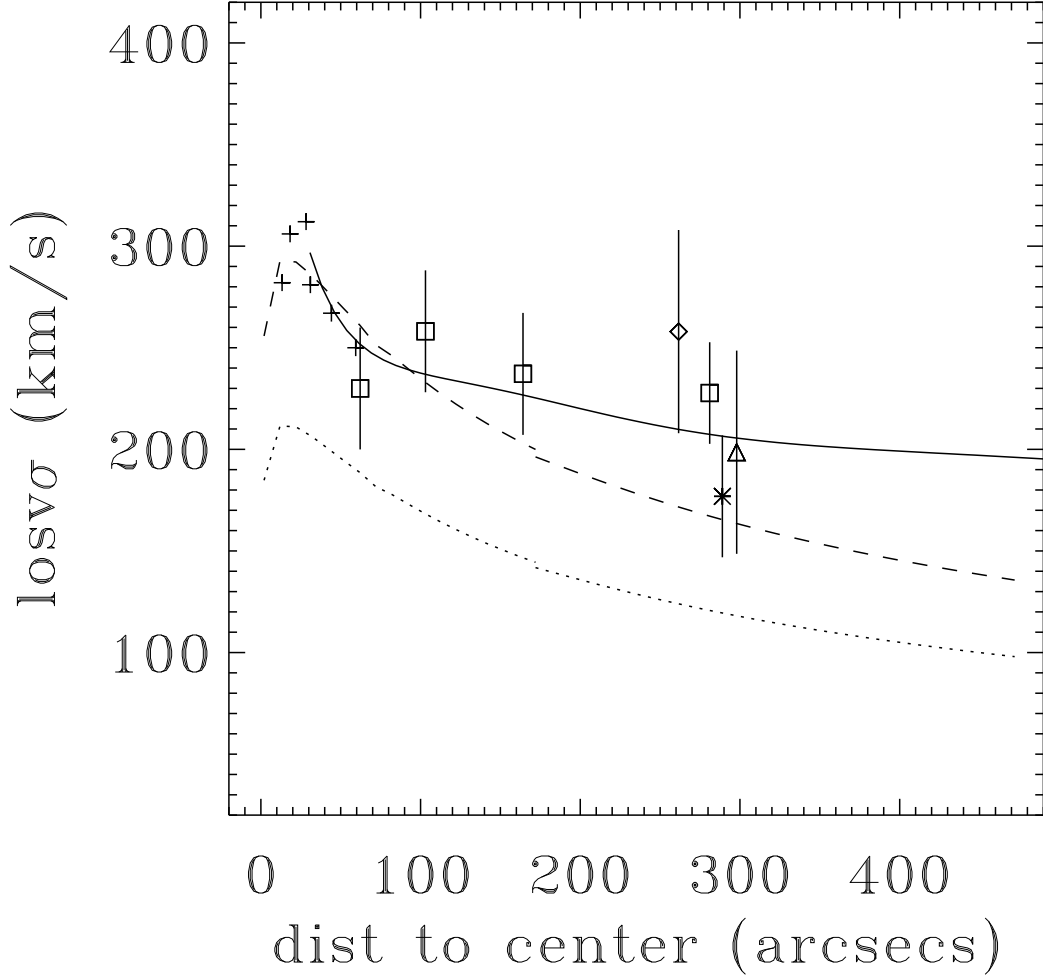


Fig. 12.— $\text{LOS}\sigma$ plotted as a function of average angular distance to the center of M 60. The PNs were divided into 4 regions, as explained in the text. These 4 data points are represented as squares. In addition, there is a diamond for PNs with large positive y , a triangle for PNs with large negative y , and an asterisk for PNs with large positive x . Plus signs are major axis, long-slit absorption-line data (Fisher et al. 1995, Pinkney et al. 2003). The dotted line represents the analytical model of Hernquist (1990), with a constant M/L ratio, a total mass of $6 \times 10^{11} M_{\odot}$, and $R_e = 128''$. The dashed line is the same kind of model, but with a higher mass of $1.15 \times 10^{12} M_{\odot}$. The solid line is a two-component Hernquist mass distribution, as described in the text.

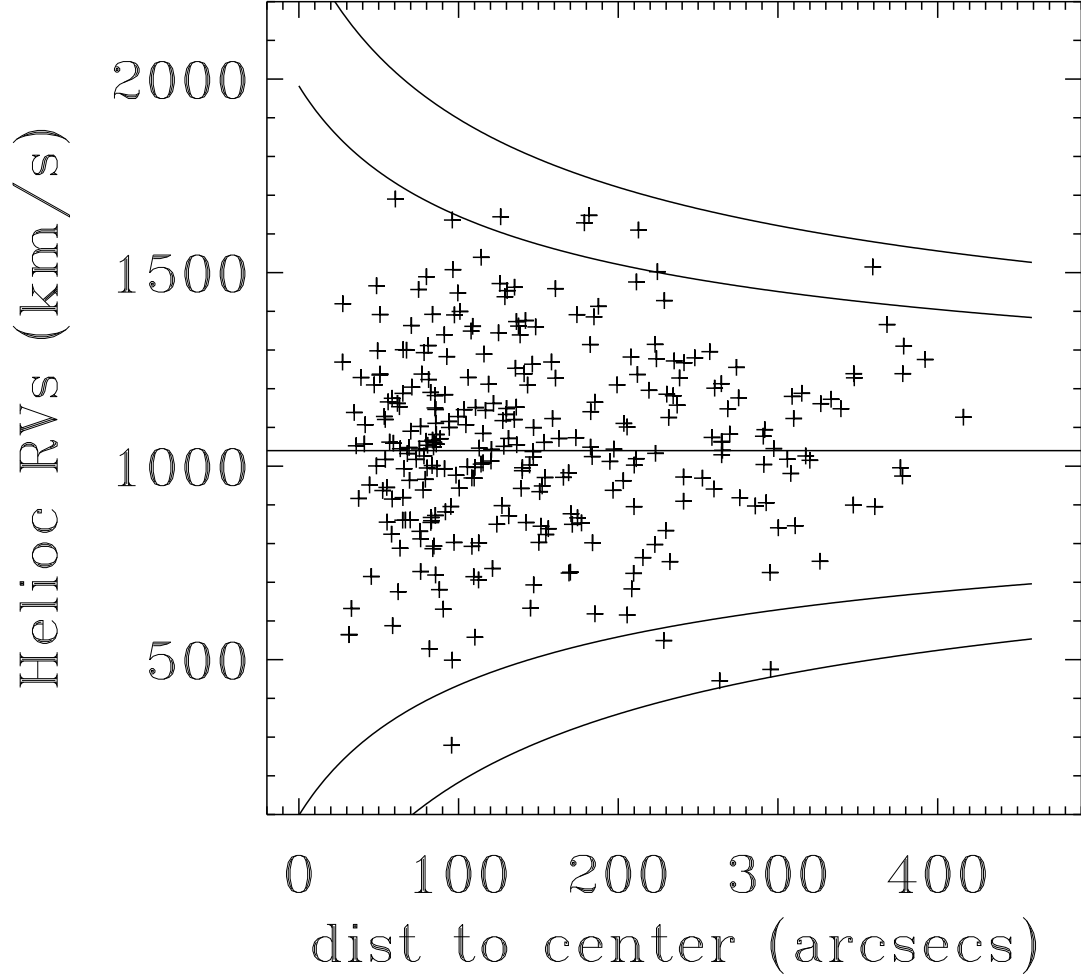


Fig. 13.— Individual PN radial velocities plotted as a function of angular distance from the center of M 60. The solid lines are escape velocities for Hernquist models with total masses $1.2 \times 10^{12} M_{\odot}$ (outer lines) and $6 \times 10^{11} M_{\odot}$ (inner lines).

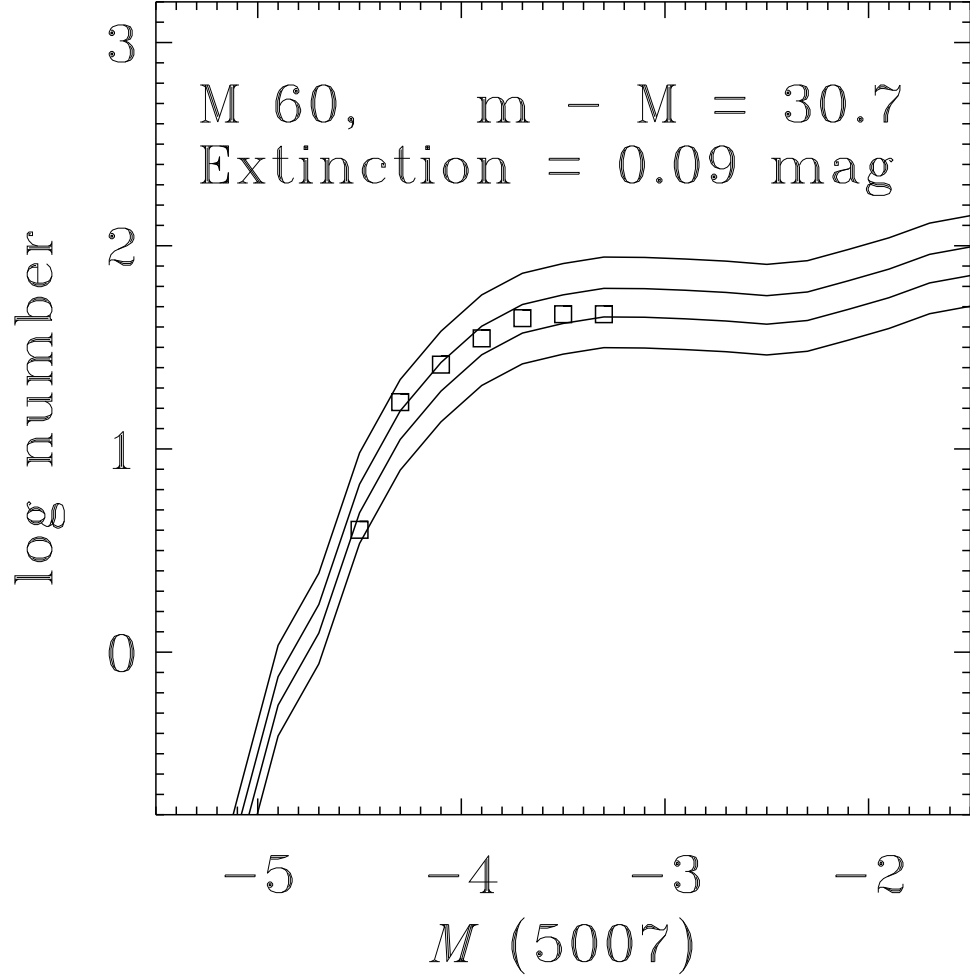


Fig. 14.— Observed [O III] $\lambda 5007$ PNLF of M 60 (squares), with the statistically complete sample of 218 PNs binned into 0.2 mag intervals. The apparent magnitudes $m(5007)$ have been transformed into absolute magnitudes $M(5007)$ by adopting an extinction correction of 0.09 mag and a distance modulus $m - M = 30.7$. The four lines are PNLF simulations (Méndez and Soffner 1997) for four different total PN population sizes: 2400, 3400, 4700, and 6700 PNs. We estimate the best-fit sample size to be 4000. From this sample size it is possible to estimate the PN formation rate (see the text).

Table 1. FORS2 observations and calibrations

| FORS2 Field | Configuration | FORS2 CCD Frame Ident (Chip 1) | Exp (s) | Air Mass ^a |
|-----------------|---------------|--------------------------------|---------|-----------------------|
| Abell 35 + mask | On+grism | FORS2.2007-06-09T23:15:19.194 | 300 | 1.03 |
| Abell 35 + mask | On-band | FORS2.2007-06-09T23:24:38.708 | 240 | 1.03 |
| M 60 Field 2 | Off-band | FORS2.2007-06-09T23:48:15.900 | 600 | 1.24 |
| M 60 Field 2 | On-band | FORS2.2007-06-09T23:59:17.372 | 1700 | 1.24 |
| M 60 Field 2 | On+grism | FORS2.2007-06-10T00:29:03.342 | 2100 | 1.24 |
| M 60 Field 2 | Off-band | FORS2.2007-06-10T01:05:46.856 | 600 | 1.27 |
| M 60 Field 2 | On-band | FORS2.2007-06-10T01:16:46.678 | 1700 | 1.30 |
| M 60 Field 2 | On+grism | FORS2.2007-06-10T01:46:34.724 | 2100 | 1.36 |
| M 60 Field 2 | Off-band | FORS2.2007-06-10T02:23:19.535 | 600 | 1.49 |
| M 60 Field 2 | On-band | FORS2.2007-06-10T02:34:18.977 | 2000 | 1.55 |
| M 60 Field 2 | On+grism | FORS2.2007-06-10T03:09:03.997 | 2400 | 1.79 |
| Abell 35 + mask | On-band | FORS2.2007-06-10T22:56:45.928 | 240 | 1.06 |
| Abell 35 + mask | On+grism | FORS2.2007-06-10T23:02:44.136 | 300 | 1.05 |
| M 60 Field 1 | Off-band | FORS2.2007-06-10T23:29:38.634 | 600 | 1.26 |
| M 60 Field 1 | On-band | FORS2.2007-06-10T23:40:54.568 | 1700 | 1.25 |
| M 60 Field 1 | On+grism | FORS2.2007-06-11T00:10:52.768 | 2100 | 1.24 |
| M 60 Field 1 | Off-band | FORS2.2007-06-11T00:47:48.811 | 600 | 1.26 |
| M 60 Field 1 | On-band | FORS2.2007-06-11T00:58:59.683 | 1700 | 1.27 |
| M 60 Field 1 | On+grism | FORS2.2007-06-11T01:28:57.702 | 2100 | 1.30 |
| M 60 Field 1 | Off-band | FORS2.2007-06-11T02:05:54.744 | 600 | 1.44 |
| M 60 Field 1 | On-band | FORS2.2007-06-11T02:17:07.606 | 1700 | 1.50 |
| M 60 Field 1 | On+grism | FORS2.2007-06-11T02:47:07.045 | 2100 | 1.65 |

^athe air masses correspond to the middle of each exposure

Table 2. FOCAS observations and calibrations

| FOCAS Field | Configuration | FOCAS Ident (Chip 1) | Exp (s) | Air Mass ^a |
|-----------------|---------------|----------------------|---------|-----------------------|
| M 60 Field 1 | Off-band | 88415 | 220 | 1.01 |
| M 60 Field 1 | On-band | 88417 | 2700 | 1.01 |
| M 60 Field 1 | On+grism | 88419 | 2700 | 1.04 |
| M 60 Field 1 | On+grism | 88421 | 2700 | 1.11 |
| G 138 - 31 | On-band | 88429 | 60 | 1.02 |
| G 138 - 31 | On-band | 88437 | 120 | 1.02 |
| M 60 Field 1 | Off-band | 88523 | 220 | 1.56 |
| M 60 Field 1 | On-band | 88525 | 2700 | 1.52 |
| M 60 Field 1 | On+grism | 88527 | 2700 | 1.27 |
| M 60 Field 1 | On+grism | 88529 | 2700 | 1.12 |
| M 60 Field 1 | Off-band | 88535 | 220 | 1.04 |
| M 60 Field 1 | On-band | 88537 | 2700 | 1.03 |
| M 60 Field 1 | On+grism | 88539 | 2700 | 1.01 |
| M 60 Field 1 | On+grism | 88541 | 2700 | 1.03 |
| M 60 Field 1 | Off-band | 88547 | 220 | 1.11 |
| M 60 Field 1 | On-band | 88549 | 2700 | 1.12 |
| M 60 Field 1 | On+grism | 88551 | 2700 | 1.26 |
| M 60 Field 1 | Off-band | 95465 | 220 | 1.01 |
| M 60 Field 1 | On-band | 95469 | 2700 | 1.02 |
| M 60 Field 1 | On+grism | 95471 | 2700 | 1.07 |
| M 60 Field 1 | On+grism | 95473 | 2700 | 1.16 |
| M 60 Field 1 | On+grism | 95479 | 2700 | 1.38 |
| G 138 - 31 | On-band | 95481 | 60 | 1.02 |
| G 138 - 31 | On-band | 95483 | 60 | 1.02 |
| M 60 Field 3 | Off-band | 95581 | 220 | 1.27 |
| M 60 Field 3 | On-band | 95583 | 2700 | 1.25 |
| M 60 Field 3 | On+grism | 95585 | 2700 | 1.11 |
| M 60 Field 3 | On+grism | 95587 | 2700 | 1.04 |
| Abell 35 + mask | On-band | 95597 | 300 | 1.36 |
| Abell 35 + mask | On+grism | 95599 | 600 | 1.36 |
| M 60 Field 3 | Off-band | 95603 | 220 | 1.02 |

Table 2—Continued

| FOCAS Field | Configuration | FOCAS Ident (Chip 1) | Exp (s) | Air Mass ^a |
|--------------|---------------|----------------------|---------|-----------------------|
| M 60 Field 3 | On-band | 95605 | 2700 | 1.03 |
| M 60 Field 3 | On+grism | 95607 | 2700 | 1.08 |
| M 60 Field 3 | On+grism | 95609 | 2200 | 1.20 |
| M 60 Field 3 | Off-band | 95615 | 220 | 1.40 |
| M 60 Field 3 | On-band | 95617 | 2700 | 1.43 |
| G 138 - 31 | On-band | 95621 | 60 | 1.02 |
| G 138 - 31 | On-band | 95623 | 60 | 1.02 |

^athe air masses correspond to the middle of each exposure

Table 3. PN Candidates in M 60

| ID | α (J2000) | | | δ (J2000) | | | x , G | y , G | Helioc. RV (km s ⁻¹) | m (5007) |
|------|---------------------|----|-------|---------------------|----|------|---------|---------|-------------------------------------|---------------|
| 5 | 12 | 43 | 34.65 | 11 | 35 | 27.2 | -112. | 112. | 1269. | 26.4 |
| 7 | 12 | 43 | 34.90 | 11 | 37 | 33.6 | -141. | 235. | 1255. | 27.1 |
| 10 | 12 | 43 | 35.25 | 11 | 35 | 48.8 | -108. | 135. | 1073. | 27.1 |
| 12 | 12 | 43 | 35.59 | 11 | 34 | 25.9 | -82. | 56. | 1128. | 26.8 |
| 13 | 12 | 43 | 35.86 | 11 | 36 | 2.2 | -103. | 151. | 1049. | 26.6 |
| 15 | 12 | 43 | 35.90 | 11 | 34 | 0.2 | -71. | 33. | 1293. | 28.0 |
| 16 | 12 | 43 | 35.98 | 11 | 35 | 24.6 | -92. | 115. | 1100. | 27.0 |
| 18 | 12 | 43 | 36.38 | 11 | 35 | 10.0 | -82. | 102. | 1072. | 27.5 |
| 20 | 12 | 43 | 36.46 | 11 | 38 | 15.5 | -129. | 282. | 1123. | 27.5 |
| 23 | 12 | 43 | 36.89 | 11 | 35 | 49.2 | -85. | 142. | 971. | 27.1 |
| 26 | 12 | 43 | 37.44 | 11 | 37 | 24.5 | -102. | 236. | 1296. | 27.9 |
| 28 | 12 | 43 | 37.94 | 11 | 34 | 20.8 | -48. | 61. | 1238. | 26.9 |
| 29 | 12 | 43 | 37.97 | 11 | 34 | 37.7 | -52. | 77. | 1283. | 26.8 |
| 30 | 12 | 43 | 37.99 | 11 | 34 | 27.2 | -48. | 67. | 855. | 26.9 |
| 32 | 12 | 43 | 38.09 | 11 | 34 | 28.1 | -47. | 68. | 859. | 27.5 |
| 35 | 12 | 43 | 38.62 | 11 | 34 | 42.0 | -43. | 84. | 1100. | 27.5 |
| 36 | 12 | 43 | 38.64 | 11 | 34 | 28.7 | -40. | 71. | 1224. | 26.7 |
| 38 | 12 | 43 | 38.74 | 11 | 33 | 47.2 | -28. | 31. | 1107. | 26.3 |
| 40 | 12 | 43 | 38.81 | 11 | 37 | 10.5 | -79. | 228. | 1267. | 27.2 |
| 2005 | 12 | 43 | 38.85 | 11 | 31 | 55.7 | 3. | -76. | 812. | -1.0 |
| 42 | 12 | 43 | 38.88 | 11 | 34 | 30.9 | -37. | 74. | 1190. | 27.2 |
| 43 | 12 | 43 | 38.90 | 11 | 34 | 52.2 | -42. | 94. | 1146. | 26.7 |
| 44 | 12 | 43 | 38.93 | 11 | 34 | 28.8 | -36. | 72. | 995. | 26.8 |
| 45 | 12 | 43 | 39.07 | 11 | 36 | 12.2 | -60. | 172. | 1141. | 27.3 |

Table 3—Continued

| ID | α (J2000) | | | δ (J2000) | | | x , G | y , G | Helioc. RV (km s ⁻¹) | m (5007) |
|------|---------------------|----|-------|---------------------|----|------|---------|---------|-------------------------------------|---------------|
| 2008 | 12 | 43 | 39.13 | 11 | 32 | 17.5 | 1. | -54. | 1121. | -1.0 |
| 48 | 12 | 43 | 39.31 | 11 | 34 | 40.5 | -33. | 85. | 1339. | 27.6 |
| 2009 | 12 | 43 | 39.35 | 11 | 32 | 30.1 | 1. | -41. | 1057. | -1.0 |
| 53 | 12 | 43 | 39.43 | 11 | 34 | 33.0 | -30. | 78. | 1002. | 27.3 |
| 2010 | 12 | 43 | 39.54 | 11 | 30 | 54.6 | 28. | -133. | 1253. | -1.0 |
| 2011 | 12 | 43 | 39.54 | 11 | 31 | 34.3 | 18. | -94. | 499. | -1.0 |
| 1090 | 12 | 43 | 39.48 | 11 | 32 | 39.5 | 0. | -32. | 565. | -1.0 |
| 59 | 12 | 43 | 39.65 | 11 | 33 | 58.3 | -18. | 45. | 1000. | 27.0 |
| 63 | 12 | 43 | 39.77 | 11 | 37 | 35.2 | -72. | 255. | 1041. | 27.0 |
| 2014 | 12 | 43 | 39.89 | 11 | 31 | 19.9 | 27. | -107. | 558. | -1.0 |
| 70 | 12 | 43 | 40.12 | 11 | 32 | 38.8 | 10. | -30. | 565. | 27.0 |
| 71 | 12 | 43 | 40.23 | 11 | 34 | 31.7 | -18. | 80. | 528. | 26.9 |
| 73 | 12 | 43 | 40.32 | 11 | 33 | 44.4 | -4. | 34. | 1139. | 26.7 |
| 74 | 12 | 43 | 40.53 | 11 | 31 | 52.1 | 28. | -73. | 1026. | 27.0 |
| 75 | 12 | 43 | 40.53 | 11 | 32 | 16.5 | 21. | -50. | 1017. | 26.6 |
| 76 | 12 | 43 | 40.56 | 11 | 31 | 13.4 | 38. | -110. | 1144. | 26.7 |
| 77 | 12 | 43 | 40.56 | 11 | 32 | 12.5 | 23. | -53. | 824. | 28.0 |
| 78 | 12 | 43 | 40.70 | 11 | 33 | 35.5 | 3. | 27. | 1420. | 26.5 |
| 79 | 12 | 43 | 40.75 | 11 | 32 | 9.3 | 26. | -56. | 1162. | 27.2 |
| 80 | 12 | 43 | 40.79 | 11 | 32 | 0.6 | 29. | -64. | 1363. | 26.5 |
| 81 | 12 | 43 | 40.80 | 11 | 34 | 9.3 | -4. | 60. | 1690. | 26.9 |
| 83 | 12 | 43 | 41.01 | 11 | 31 | 46.2 | 36. | -77. | 1150. | 27.4 |
| 84 | 12 | 43 | 40.97 | 11 | 34 | 14.3 | -3. | 66. | 993. | 27.5 |
| 85 | 12 | 43 | 41.06 | 11 | 34 | 16.1 | -2. | 68. | 1032. | 27.3 |

Table 3—Continued

| ID | α (J2000) | | | δ (J2000) | | | x , G | y , G | Helioc. RV (km s ⁻¹) | m (5007) |
|------|---------------------|----|-------|---------------------|----|------|---------|---------|-------------------------------------|---------------|
| 86 | 12 | 43 | 41.11 | 11 | 36 | 34.9 | -37. | 202. | 1101. | 28.0 |
| 87 | 12 | 43 | 41.14 | 11 | 35 | 31.3 | -20. | 141. | 854. | 27.0 |
| 88 | 12 | 43 | 41.21 | 11 | 32 | 22.4 | 30. | -41. | 1392. | 27.7 |
| 89 | 12 | 43 | 41.28 | 11 | 33 | 30.0 | 13. | 24. | 1269. | 26.7 |
| 92 | 12 | 43 | 41.40 | 11 | 32 | 23.5 | 32. | -40. | 1238. | 27.4 |
| 93 | 12 | 43 | 41.43 | 11 | 36 | 51.9 | -37. | 220. | 797. | 27.1 |
| 2021 | 12 | 43 | 41.50 | 11 | 30 | 22.6 | 65. | -156. | 983. | -1.0 |
| 95 | 12 | 43 | 41.51 | 11 | 31 | 47.0 | 43. | -74. | 1057. | 27.4 |
| 96 | 12 | 43 | 41.55 | 11 | 32 | 6.7 | 38. | -55. | 1299. | 27.2 |
| 97 | 12 | 43 | 41.57 | 11 | 32 | 42.5 | 29. | -21. | 1053. | -1.0 |
| 98 | 12 | 43 | 41.57 | 11 | 34 | 15.3 | 5. | 69. | 963. | 27.7 |
| 100 | 12 | 43 | 41.64 | 11 | 37 | 32.4 | -45. | 260. | 446. | 26.9 |
| 101 | 12 | 43 | 41.69 | 11 | 36 | 51.9 | -33. | 221. | 1033. | 27.9 |
| 102 | 12 | 43 | 41.69 | 11 | 35 | 3.2 | -5. | 116. | 1290. | 26.6 |
| 103 | 12 | 43 | 41.76 | 11 | 34 | 20.9 | 7. | 75. | 1044. | 27.5 |
| 104 | 12 | 43 | 41.81 | 11 | 36 | 36.8 | -28. | 207. | 683. | 27.8 |
| 105 | 12 | 43 | 41.83 | 11 | 32 | 18.2 | 39. | -43. | 1175. | 27.2 |
| 106 | 12 | 43 | 41.85 | 11 | 34 | 6.8 | 12. | 62. | 1153. | 27.5 |
| 107 | 12 | 43 | 41.90 | 11 | 31 | 49.2 | 48. | -71. | 873. | -1.0 |
| 108 | 12 | 43 | 41.93 | 11 | 31 | 48.7 | 48. | -71. | 1082. | -1.0 |
| 110 | 12 | 43 | 41.98 | 11 | 32 | 54.6 | 32. | -7. | 632. | 26.8 |
| 111 | 12 | 43 | 41.98 | 11 | 34 | 24.4 | 9. | 79. | 1489. | 27.1 |
| 112 | 12 | 43 | 42.02 | 11 | 32 | 37.2 | 37. | -24. | 952. | -1.0 |
| 113 | 12 | 43 | 42.04 | 11 | 32 | 47.5 | 35. | -14. | 916. | 26.3 |

Table 3—Continued

| ID | α (J2000) | | | δ (J2000) | | | x , G | y , G | Helioc. RV (km s ⁻¹) | m (5007) |
|-----|---------------------|----|-------|---------------------|----|------|---------|---------|-------------------------------------|---------------|
| 114 | 12 | 43 | 42.06 | 11 | 31 | 18.8 | 58. | -100. | 1085. | 27.3 |
| 115 | 12 | 43 | 42.06 | 11 | 31 | 44.0 | 52. | -75. | 993. | 26.9 |
| 116 | 12 | 43 | 42.27 | 11 | 32 | 28.2 | 43. | -32. | 1128. | -1.0 |
| 117 | 12 | 43 | 42.30 | 11 | 32 | 26.6 | 44. | -33. | 945. | 26.7 |
| 118 | 12 | 43 | 42.41 | 11 | 36 | 34.9 | -19. | 207. | 1282. | 27.9 |
| 119 | 12 | 43 | 42.47 | 11 | 34 | 10.8 | 19. | 68. | 1204. | 26.7 |
| 122 | 12 | 43 | 42.50 | 11 | 32 | 57.3 | 39. | -3. | 1229. | -1.0 |
| 124 | 12 | 43 | 42.58 | 11 | 34 | 24.6 | 17. | 82. | 1067. | 27.6 |
| 125 | 12 | 43 | 42.55 | 11 | 32 | 4.2 | 53. | -54. | 832. | 26.7 |
| 126 | 12 | 43 | 42.67 | 11 | 32 | 16.1 | 52. | -42. | 860. | 27.1 |
| 127 | 12 | 43 | 42.77 | 11 | 35 | 56.3 | -4. | 171. | 850. | 26.8 |
| 128 | 12 | 43 | 42.77 | 11 | 34 | 36.0 | 17. | 94. | 896. | 27.5 |
| 129 | 12 | 43 | 42.94 | 11 | 31 | 53.3 | 62. | -63. | 681. | 27.2 |
| 130 | 12 | 43 | 43.20 | 11 | 31 | 57.4 | 64. | -58. | 993. | 26.7 |
| 131 | 12 | 43 | 43.25 | 11 | 34 | 21.2 | 28. | 81. | 1111. | 27.6 |
| 132 | 12 | 43 | 43.27 | 11 | 36 | 0.4 | 2. | 177. | 853. | 26.8 |
| 133 | 12 | 43 | 43.36 | 11 | 33 | 7.6 | 48. | 10. | 1298. | 27.1 |
| 134 | 12 | 43 | 43.43 | 11 | 33 | 24.4 | 45. | 27. | 937. | 26.5 |
| 136 | 12 | 43 | 43.49 | 11 | 32 | 45.6 | 56. | -10. | 1062. | -1.0 |
| 137 | 12 | 43 | 43.58 | 11 | 35 | 37.1 | 13. | 156. | 838. | 27.0 |
| 138 | 12 | 43 | 43.63 | 11 | 35 | 15.4 | 19. | 135. | 1374. | 27.8 |
| 139 | 12 | 43 | 43.73 | 11 | 32 | 48.9 | 58. | -6. | 588. | -1.0 |
| 140 | 12 | 43 | 43.75 | 11 | 37 | 0.4 | -6. | 237. | 1158. | 27.6 |
| 141 | 12 | 43 | 43.79 | 11 | 33 | 4.3 | 55. | 9. | 1166. | 26.6 |

Table 3—Continued

| ID | α (J2000) | | | δ (J2000) | | | x , G | y , G | Helioc. RV (km s ⁻¹) | m (5007) |
|-----|---------------------|----|-------|---------------------|----|------|---------|---------|-------------------------------------|---------------|
| 142 | 12 | 43 | 43.80 | 11 | 32 | 52.8 | 58. | -2. | 915. | 26.5 |
| 143 | 12 | 43 | 43.90 | 11 | 30 | 48.9 | 92. | -122. | 949. | 27.6 |
| 144 | 12 | 43 | 44.06 | 11 | 37 | 55.0 | -16. | 291. | 1004. | 27.1 |
| 145 | 12 | 43 | 44.01 | 11 | 32 | 42.3 | 64. | -12. | 919. | 26.4 |
| 146 | 12 | 43 | 44.13 | 11 | 34 | 8.9 | 43. | 72. | 1062. | 27.4 |
| 147 | 12 | 43 | 44.18 | 11 | 35 | 6.1 | 29. | 128. | 872. | 27.2 |
| 149 | 12 | 43 | 44.22 | 11 | 33 | 4.2 | 61. | 10. | 675. | -1.0 |
| 150 | 12 | 43 | 44.36 | 11 | 31 | 21.2 | 90. | -89. | 1644. | 27.7 |
| 151 | 12 | 43 | 44.35 | 11 | 32 | 44.1 | 68. | -8. | 1048. | 27.7 |
| 152 | 12 | 43 | 44.40 | 11 | 33 | 45.0 | 53. | 50. | 1018. | 27.5 |
| 153 | 12 | 43 | 44.46 | 11 | 31 | 44.5 | 86. | -66. | 1349. | 27.6 |
| 154 | 12 | 43 | 44.49 | 11 | 32 | 23.7 | 76. | -28. | 1054. | 27.5 |
| 155 | 12 | 43 | 44.59 | 11 | 37 | 54.7 | -8. | 292. | 906. | 27.7 |
| 156 | 12 | 43 | 44.66 | 11 | 33 | 43.5 | 58. | 50. | 728. | 27.3 |
| 157 | 12 | 43 | 44.74 | 11 | 37 | 0.6 | 8. | 241. | 972. | 27.1 |
| 158 | 12 | 43 | 44.81 | 11 | 32 | 37.4 | 77. | -13. | 938. | 27.1 |
| 159 | 12 | 43 | 44.88 | 11 | 31 | 48.8 | 90. | -60. | 793. | 27.7 |
| 160 | 12 | 43 | 44.90 | 11 | 31 | 43.6 | 92. | -65. | 706. | 27.5 |
| 161 | 12 | 43 | 45.10 | 11 | 33 | 23.2 | 69. | 32. | 1103. | 27.1 |
| 162 | 12 | 43 | 45.34 | 11 | 30 | 34.2 | 116. | -130. | 866. | 27.7 |
| 163 | 12 | 43 | 45.36 | 11 | 32 | 15.8 | 90. | -32. | 279. | 27.0 |
| 164 | 12 | 43 | 45.41 | 11 | 32 | 46.6 | 83. | -2. | 867. | -1.0 |
| 165 | 12 | 43 | 45.42 | 11 | 32 | 12.3 | 92. | -35. | 977. | 26.6 |
| 166 | 12 | 43 | 45.44 | 11 | 31 | 38.0 | 101. | -68. | 1162. | 27.1 |

Table 3—Continued

| ID | α (J2000) | | | δ (J2000) | | | x , G | y , G | Helioc. RV (km s ⁻¹) | m (5007) |
|-----|---------------------|----|-------|---------------------|----|------|---------|---------|-------------------------------------|---------------|
| 168 | 12 | 43 | 45.57 | 11 | 32 | 51.4 | 84. | 3. | 787. | -1.0 |
| 169 | 12 | 43 | 45.61 | 11 | 31 | 33.2 | 105. | -72. | 898. | 27.8 |
| 170 | 12 | 43 | 45.62 | 11 | 32 | 33.0 | 89. | -14. | 630. | 27.0 |
| 171 | 12 | 43 | 45.67 | 11 | 32 | 14.0 | 95. | -33. | 943. | 27.6 |
| 172 | 12 | 43 | 45.89 | 11 | 31 | 48.6 | 105. | -56. | 1212. | 27.5 |
| 173 | 12 | 43 | 45.93 | 11 | 32 | 42.4 | 91. | -4. | 1185. | 27.4 |
| 174 | 12 | 43 | 46.03 | 11 | 34 | 22.1 | 67. | 92. | 1540. | 27.5 |
| 175 | 12 | 43 | 46.07 | 11 | 30 | 0.4 | 135. | -160. | 723. | 27.4 |
| 177 | 12 | 43 | 46.08 | 11 | 31 | 57.1 | 105. | -47. | 1008. | 27.6 |
| 178 | 12 | 43 | 46.10 | 11 | 36 | 15.0 | 39. | 202. | 616. | 26.8 |
| 180 | 12 | 43 | 46.14 | 11 | 32 | 8.0 | 103. | -37. | 714. | 27.0 |
| 181 | 12 | 43 | 46.17 | 11 | 32 | 55.5 | 91. | 9. | 882. | -1.0 |
| 182 | 12 | 43 | 46.27 | 11 | 31 | 11.4 | 120. | -91. | 803. | 27.7 |
| 183 | 12 | 43 | 46.35 | 11 | 29 | 34.3 | 146. | -184. | 1272. | 26.9 |
| 185 | 12 | 43 | 46.52 | 11 | 33 | 3.0 | 94. | 18. | 1636. | 27.0 |
| 186 | 12 | 43 | 46.56 | 11 | 31 | 35.5 | 118. | -66. | 1462. | 26.9 |
| 187 | 12 | 43 | 46.53 | 11 | 32 | 55.1 | 97. | 10. | 803. | -1.0 |
| 189 | 12 | 43 | 46.82 | 11 | 34 | 23.0 | 78. | 96. | 850. | 27.6 |
| 190 | 12 | 43 | 46.80 | 11 | 37 | 43.1 | 26. | 290. | 1077. | 27.5 |
| 191 | 12 | 43 | 46.80 | 11 | 32 | 36.0 | 105. | -7. | 998. | -1.0 |
| 193 | 12 | 43 | 46.84 | 11 | 30 | 23.2 | 140. | -135. | 1012. | 27.2 |
| 194 | 12 | 43 | 47.11 | 11 | 35 | 14.9 | 69. | 148. | 1072. | 27.3 |
| 196 | 12 | 43 | 47.21 | 11 | 30 | 16.7 | 147. | -140. | 962. | 27.0 |
| 197 | 12 | 43 | 47.22 | 11 | 30 | 39.9 | 141. | -118. | 802. | 27.6 |

Table 3—Continued

| ID | α (J2000) | | | δ (J2000) | | | x , G | y , G | Helioc. RV (km s ⁻¹) | m (5007) |
|------|---------------------|----|-------|---------------------|----|------|---------|---------|-------------------------------------|---------------|
| 198 | 12 | 43 | 47.13 | 11 | 32 | 27.6 | 112. | -14. | 1046. | 26.8 |
| 199 | 12 | 43 | 47.21 | 11 | 32 | 41.3 | 110. | -0. | 969. | 27.5 |
| 200 | 12 | 43 | 47.25 | 11 | 34 | 22.8 | 84. | 98. | 1438. | 27.2 |
| 201 | 12 | 43 | 47.26 | 11 | 31 | 58.7 | 122. | -41. | 1051. | 27.4 |
| 202 | 12 | 43 | 47.26 | 11 | 32 | 51.2 | 108. | 9. | 970. | 27.9 |
| 204 | 12 | 43 | 47.32 | 11 | 30 | 8.1 | 151. | -148. | 1476. | 27.5 |
| 205 | 12 | 43 | 47.49 | 11 | 30 | 49.2 | 143. | -108. | 1629. | 27.4 |
| 206 | 12 | 43 | 47.55 | 11 | 31 | 51.2 | 128. | -47. | 1152. | 27.1 |
| 208 | 12 | 43 | 47.69 | 11 | 32 | 53.7 | 113. | 14. | 1005. | -1.0 |
| 209 | 12 | 43 | 48.00 | 11 | 31 | 42.7 | 136. | -54. | 1038. | 27.2 |
| 210 | 12 | 43 | 48.04 | 11 | 30 | 32.1 | 155. | -122. | 1044. | 27.2 |
| 212 | 12 | 43 | 48.14 | 11 | 32 | 56.9 | 119. | 18. | 1013. | -1.0 |
| 214 | 12 | 43 | 48.26 | 11 | 33 | 40.2 | 109. | 61. | 1344. | 27.5 |
| 215 | 12 | 43 | 48.46 | 11 | 31 | 38.0 | 144. | -57. | 823. | 28.0 |
| 216 | 12 | 43 | 48.54 | 11 | 35 | 4.8 | 92. | 143. | 726. | 26.6 |
| 217 | 12 | 43 | 48.52 | 11 | 32 | 7.2 | 137. | -28. | 996. | 27.0 |
| 218 | 12 | 43 | 48.54 | 11 | 34 | 50.4 | 95. | 129. | 1227. | 27.4 |
| 219 | 12 | 43 | 48.55 | 11 | 33 | 17.0 | 120. | 39. | 1472. | 27.4 |
| 221 | 12 | 43 | 48.63 | 11 | 34 | 0.3 | 110. | 81. | 1055. | 28.2 |
| 1126 | 12 | 43 | 48.85 | 11 | 33 | 10.2 | 126. | 34. | 1149. | -1.0 |
| 224 | 12 | 43 | 48.97 | 11 | 29 | 25.5 | 185. | -183. | 1201. | 27.1 |
| 225 | 12 | 43 | 49.08 | 11 | 32 | 36.7 | 138. | 2. | 1362. | 27.3 |
| 226 | 12 | 43 | 49.18 | 11 | 36 | 14.5 | 82. | 213. | 549. | 28.0 |
| 227 | 12 | 43 | 49.25 | 11 | 36 | 57.0 | 73. | 254. | 1213. | 27.3 |

Table 3—Continued

| ID | α (J2000) | | | δ (J2000) | | | x , G | y , G | Helioc. RV (km s ⁻¹) | m (5007) |
|-----|---------------------|----|-------|---------------------|----|------|---------|---------|-------------------------------------|---------------|
| 228 | 12 | 43 | 49.42 | 11 | 33 | 30.2 | 128. | 55. | 988. | 27.7 |
| 230 | 12 | 43 | 49.54 | 11 | 32 | 25.8 | 147. | -6. | 693. | 26.3 |
| 231 | 12 | 43 | 49.54 | 11 | 37 | 30.0 | 68. | 287. | 475. | 27.3 |
| 232 | 12 | 43 | 49.78 | 11 | 33 | 37.3 | 132. | 64. | 1264. | 27.2 |
| 234 | 12 | 43 | 49.85 | 11 | 33 | 19.1 | 138. | 46. | 633. | -1.0 |
| 235 | 12 | 43 | 50.17 | 11 | 34 | 56.7 | 117. | 142. | 1025. | 27.6 |
| 236 | 12 | 43 | 50.50 | 11 | 29 | 28.7 | 206. | -174. | 1083. | 27.2 |
| 238 | 12 | 43 | 50.90 | 11 | 38 | 18.3 | 75. | 339. | 1239. | 27.1 |
| 239 | 12 | 43 | 51.36 | 11 | 32 | 35.6 | 170. | 10. | 877. | -1.0 |
| 240 | 12 | 43 | 51.41 | 11 | 29 | 30.6 | 219. | -168. | 918. | 27.5 |
| 241 | 12 | 43 | 51.40 | 11 | 31 | 0.1 | 195. | -82. | 1237. | 27.3 |
| 242 | 12 | 43 | 51.47 | 11 | 32 | 56.2 | 166. | 30. | 724. | 27.2 |
| 243 | 12 | 43 | 51.42 | 11 | 31 | 3.8 | 195. | -78. | 1003. | 26.8 |
| 244 | 12 | 43 | 51.52 | 11 | 34 | 50.1 | 138. | 141. | 938. | 27.3 |
| 246 | 12 | 43 | 51.98 | 11 | 29 | 52.2 | 221. | -146. | 1062. | 27.6 |
| 248 | 12 | 43 | 52.14 | 11 | 31 | 9.3 | 204. | -70. | 764. | 27.4 |
| 250 | 12 | 43 | 52.27 | 11 | 36 | 29.0 | 123. | 239. | 1148. | 27.7 |
| 251 | 12 | 43 | 52.37 | 11 | 32 | 54.1 | 180. | 32. | 1314. | 27.6 |
| 252 | 12 | 43 | 52.57 | 11 | 33 | 15.5 | 177. | 53. | 1386. | 27.0 |
| 253 | 12 | 43 | 52.61 | 11 | 30 | 25.2 | 222. | -111. | 1280. | 27.4 |
| 254 | 12 | 43 | 52.65 | 11 | 30 | 50.6 | 216. | -87. | 753. | 26.5 |
| 255 | 12 | 43 | 52.89 | 11 | 30 | 52.1 | 219. | -84. | 1182. | 27.2 |
| 257 | 12 | 43 | 53.01 | 11 | 32 | 0.2 | 203. | -18. | 1110. | 26.5 |
| 258 | 12 | 43 | 53.40 | 11 | 33 | 40.0 | 182. | 80. | 1210. | 27.8 |

Table 3—Continued

| ID | α (J2000) | | | δ (J2000) | | | x , G | y , G | Helioc. RV (km s ⁻¹) | m (5007) |
|------|---------------------|----|-------|---------------------|----|------|---------|---------|-------------------------------------|---------------|
| 259 | 12 | 43 | 53.45 | 11 | 36 | 49.1 | 134. | 263. | 725. | 26.7 |
| 260 | 12 | 43 | 53.49 | 11 | 31 | 12.9 | 222. | -62. | 1186. | 27.4 |
| 261 | 12 | 43 | 53.57 | 11 | 37 | 8.4 | 131. | 282. | 846. | 26.8 |
| 262 | 12 | 43 | 54.00 | 11 | 30 | 23.6 | 242. | -108. | 1064. | 26.8 |
| 263 | 12 | 43 | 53.99 | 11 | 32 | 27.9 | 210. | 12. | 895. | 26.8 |
| 264 | 12 | 43 | 54.02 | 11 | 31 | 42.4 | 222. | -31. | 1277. | 28.0 |
| 266 | 12 | 43 | 54.67 | 11 | 36 | 26.5 | 157. | 246. | 1094. | 27.4 |
| 267 | 12 | 43 | 54.72 | 11 | 32 | 10.0 | 224. | -2. | 1502. | 27.2 |
| 268 | 12 | 43 | 55.62 | 11 | 33 | 21.0 | 219. | 70. | 834. | 26.8 |
| 269 | 12 | 43 | 55.67 | 11 | 30 | 39.0 | 262. | -86. | 1176. | 27.3 |
| 270 | 12 | 43 | 56.42 | 11 | 29 | 47.6 | 285. | -133. | 1188. | 26.6 |
| 271 | 12 | 43 | 56.88 | 11 | 34 | 23.4 | 221. | 135. | 1074. | 27.5 |
| 273 | 12 | 43 | 57.17 | 11 | 32 | 56.2 | 247. | 52. | 969. | 27.6 |
| 274 | 12 | 43 | 57.24 | 11 | 34 | 7.9 | 230. | 122. | 941. | 26.3 |
| 275 | 12 | 43 | 57.43 | 11 | 30 | 38.8 | 286. | -80. | 1045. | 28.0 |
| 276 | 12 | 43 | 58.01 | 11 | 33 | 2.3 | 258. | 61. | 1029. | 27.8 |
| 277 | 12 | 43 | 58.84 | 11 | 31 | 58.9 | 286. | 3. | 897. | 27.5 |
| 278 | 12 | 43 | 59.21 | 11 | 30 | 45.1 | 310. | -67. | 1026. | 27.0 |
| 280 | 12 | 43 | 59.64 | 11 | 31 | 28.7 | 305. | -23. | 1018. | 27.8 |
| 281 | 12 | 44 | 0.36 | 11 | 30 | 12.8 | 335. | -94. | 1228. | 27.9 |
| 282 | 12 | 44 | 0.42 | 11 | 33 | 19.2 | 288. | 86. | 841. | 27.0 |
| 283 | 12 | 44 | 0.73 | 11 | 32 | 24.9 | 306. | 35. | 981. | 27.2 |
| 284 | 12 | 44 | 0.84 | 11 | 33 | 49.4 | 286. | 117. | 1180. | 27.5 |
| 1157 | 12 | 44 | 1.39 | 11 | 29 | 38.8 | 358. | -123. | 1310. | -1.0 |

Table 3—Continued

| ID | α (J2000) | | | δ (J2000) | | | x , G | y , G | Helioc. RV (km s ⁻¹) | m (5007) |
|------|---------------------|----|-------|---------------------|----|------|---------|---------|-------------------------------------|---------------|
| 1158 | 12 | 44 | 1.61 | 11 | 29 | 44.7 | 360. | -116. | 1239. | -1.0 |
| 287 | 12 | 44 | 1.99 | 11 | 32 | 25.7 | 324. | 41. | 754. | 27.0 |
| 288 | 12 | 44 | 2.17 | 11 | 33 | 34.3 | 308. | 108. | 1161. | 27.5 |
| 289 | 12 | 44 | 2.52 | 11 | 31 | 25.1 | 347. | -16. | 899. | 27.7 |
| 1162 | 12 | 44 | 2.57 | 11 | 33 | 42.5 | 312. | 117. | 1173. | -1.0 |
| 601 | 12 | 43 | 43.09 | 11 | 33 | 12.0 | 43. | 14. | 715. | 26.5 |
| 603 | 12 | 43 | 43.63 | 11 | 34 | 15.7 | 34. | 77. | 793. | 26.3 |
| 605 | 12 | 43 | 43.95 | 11 | 33 | 48.6 | 46. | 52. | 861. | 26.7 |
| 608 | 12 | 43 | 44.43 | 11 | 33 | 4.9 | 64. | 12. | 1301. | 26.8 |
| 610 | 12 | 43 | 45.20 | 11 | 33 | 30.8 | 68. | 40. | 966. | 26.7 |
| 611 | 12 | 43 | 45.70 | 11 | 33 | 19.8 | 78. | 31. | 1050. | 26.5 |
| 612 | 12 | 43 | 45.78 | 11 | 33 | 21.1 | 79. | 33. | 719. | 26.4 |
| 613 | 12 | 43 | 47.36 | 11 | 33 | 22.2 | 101. | 40. | 1361. | 26.8 |
| 615 | 12 | 43 | 51.35 | 11 | 34 | 31.0 | 140. | 121. | 618. | 27.4 |
| 617 | 12 | 43 | 53.30 | 11 | 34 | 29.9 | 168. | 128. | 1019. | 27.4 |
| 1005 | 12 | 43 | 23.52 | 11 | 28 | 21.4 | -159. | -341. | 996. | -1.0 |
| 1016 | 12 | 43 | 27.02 | 11 | 30 | 47.0 | -147. | -188. | 1228. | -1.0 |
| 1022 | 12 | 43 | 28.20 | 11 | 31 | 6.9 | -136. | -164. | 1610. | -1.0 |
| 1023 | 12 | 43 | 28.30 | 11 | 27 | 33.4 | -79. | -370. | 974. | -1.0 |
| 1026 | 12 | 43 | 29.18 | 11 | 31 | 30.6 | -128. | -137. | 1413. | -1.0 |
| 1033 | 12 | 43 | 30.46 | 11 | 32 | 54.5 | -131. | -51. | 1239. | -1.0 |
| 1034 | 12 | 43 | 30.53 | 11 | 31 | 53.4 | -115. | -110. | 1123. | -1.0 |
| 1035 | 12 | 43 | 30.53 | 11 | 33 | 7.4 | -134. | -38. | 942. | -1.0 |
| 1036 | 12 | 43 | 30.60 | 11 | 33 | 20.2 | -136. | -26. | 1339. | -1.0 |

Table 3—Continued

| ID | α (J2000) | | | δ (J2000) | | | x , G | y , G | Helioc. RV (km s ⁻¹) | m (5007) |
|------|---------------------|----|-------|---------------------|----|------|---------|---------|-------------------------------------|---------------|
| 1037 | 12 | 43 | 30.94 | 11 | 27 | 34.8 | -42. | -358. | 895. | -1.0 |
| 1038 | 12 | 43 | 31.10 | 11 | 30 | 58.7 | -92. | -161. | 1165. | -1.0 |
| 1040 | 12 | 43 | 31.30 | 11 | 31 | 54.9 | -104. | -106. | 1360. | -1.0 |
| 1043 | 12 | 43 | 31.44 | 11 | 32 | 4.3 | -104. | -96. | 1376. | -1.0 |
| 1044 | 12 | 43 | 31.61 | 11 | 32 | 29.4 | -109. | -71. | 1134. | -1.0 |
| 1045 | 12 | 43 | 31.80 | 11 | 33 | 7.1 | -116. | -34. | 1043. | -1.0 |
| 1046 | 12 | 43 | 31.85 | 11 | 31 | 49.2 | -95. | -109. | 1003. | -1.0 |
| 1047 | 12 | 43 | 32.18 | 11 | 31 | 28.1 | -85. | -128. | 1062. | -1.0 |
| 1048 | 12 | 43 | 32.28 | 11 | 31 | 42.6 | -87. | -114. | 1209. | -1.0 |
| 1049 | 12 | 43 | 32.43 | 11 | 32 | 52.7 | -103. | -46. | 802. | -1.0 |
| 1052 | 12 | 43 | 32.55 | 11 | 31 | 12.4 | -75. | -142. | 1458. | -1.0 |
| 1053 | 12 | 43 | 32.55 | 11 | 31 | 26.3 | -79. | -128. | 934. | -1.0 |
| 1054 | 12 | 43 | 32.59 | 11 | 32 | 52.4 | -101. | -45. | 997. | -1.0 |
| 1056 | 12 | 43 | 33.29 | 11 | 31 | 48.8 | -74. | -104. | 1118. | -1.0 |
| 1057 | 12 | 43 | 33.43 | 11 | 29 | 53.2 | -42. | -215. | 1196. | -1.0 |
| 1058 | 12 | 43 | 33.46 | 11 | 32 | 54.0 | -89. | -40. | 1391. | -1.0 |
| 1059 | 12 | 43 | 33.72 | 11 | 32 | 17.9 | -76. | -74. | 1229. | -1.0 |
| 1060 | 12 | 43 | 34.01 | 11 | 32 | 3.0 | -68. | -88. | 1151. | -1.0 |
| 1061 | 12 | 43 | 34.15 | 11 | 32 | 48.7 | -78. | -43. | 1071. | -1.0 |
| 1062 | 12 | 43 | 34.18 | 11 | 31 | 31.6 | -57. | -117. | 1454. | -1.0 |
| 1063 | 12 | 43 | 34.51 | 11 | 32 | 3.4 | -61. | -85. | 1107. | -1.0 |
| 1064 | 12 | 43 | 34.54 | 11 | 33 | 21.3 | -80. | -10. | 1312. | -1.0 |
| 1066 | 12 | 43 | 34.56 | 11 | 32 | 40.4 | -70. | -49. | 1182. | -1.0 |
| 1067 | 12 | 43 | 34.97 | 11 | 32 | 3.4 | -54. | -84. | 1447. | -1.0 |

Table 3—Continued

| ID | α (J2000) | | | δ (J2000) | | | x , G | y , G | Helioc. RV (km s ⁻¹) | m (5007) |
|------|---------------------|----|-------|---------------------|----|------|---------|---------|-------------------------------------|---------------|
| 1070 | 12 | 43 | 35.21 | 11 | 27 | 57.9 | 13. | -320. | 1015. | -1.0 |
| 1071 | 12 | 43 | 35.40 | 11 | 32 | 37.6 | -57. | -49. | 1456. | -1.0 |
| 1072 | 12 | 43 | 35.42 | 11 | 32 | 17.0 | -51. | -69. | 1146. | -1.0 |
| 1073 | 12 | 43 | 35.71 | 11 | 32 | 39.6 | -53. | -46. | 1090. | -1.0 |
| 1074 | 12 | 43 | 35.76 | 11 | 32 | 58.8 | -57. | -27. | 788. | -1.0 |
| 1075 | 12 | 43 | 35.81 | 11 | 29 | 35.6 | -4. | -223. | 1315. | -1.0 |
| 1076 | 12 | 43 | 35.81 | 11 | 32 | 49.0 | -54. | -36. | 1188. | -1.0 |
| 1077 | 12 | 43 | 36.34 | 11 | 31 | 21.3 | -24. | -119. | 735. | -1.0 |
| 1078 | 12 | 43 | 36.60 | 11 | 27 | 34.3 | 39. | -337. | 1148. | -1.0 |
| 1079 | 12 | 43 | 36.79 | 11 | 31 | 40.9 | -22. | -98. | 1400. | -1.0 |
| 1080 | 12 | 43 | 36.79 | 11 | 33 | 8.2 | -45. | -14. | 1210. | -1.0 |
| 1081 | 12 | 43 | 37.01 | 11 | 31 | 2.4 | -9. | -135. | 1120. | -1.0 |
| 1082 | 12 | 43 | 37.08 | 11 | 32 | 29.2 | -31. | -50. | 1059. | -1.0 |
| 1083 | 12 | 43 | 37.18 | 11 | 31 | 45.7 | -18. | -92. | 1116. | -1.0 |
| 1084 | 12 | 43 | 37.71 | 11 | 32 | 32.1 | -23. | -45. | 1235. | -1.0 |
| 1085 | 12 | 43 | 37.85 | 11 | 31 | 38.9 | -7. | -96. | 1508. | -1.0 |
| 1086 | 12 | 43 | 37.89 | 11 | 31 | 56.5 | -11. | -79. | 1064. | -1.0 |
| 1087 | 12 | 43 | 38.35 | 11 | 32 | 20.4 | -11. | -54. | 855. | -1.0 |
| 1088 | 12 | 43 | 38.62 | 11 | 32 | 25.7 | -8. | -48. | 1466. | -1.0 |
| 1089 | 12 | 43 | 38.98 | 11 | 27 | 10.9 | 78. | -351. | 1515. | -1.0 |
| 1091 | 12 | 43 | 39.84 | 11 | 29 | 18.4 | 58. | -224. | 1126. | -1.0 |
| 1092 | 12 | 43 | 40.78 | 11 | 29 | 21.4 | 70. | -218. | 1428. | -1.0 |
| 1094 | 12 | 43 | 41.64 | 11 | 29 | 10.3 | 85. | -225. | 909. | -1.0 |
| 1163 | 12 | 44 | 3.41 | 11 | 30 | 1.9 | 381. | -93. | 1276. | -1.0 |

Table 3—Continued

| ID | α (J2000) | | | δ (J2000) | | | x , G | y , G | Helioc. RV (km s ⁻¹) | m (5007) |
|------|---------------------|----|-------|---------------------|----|------|---------|---------|-------------------------------------|---------------|
| 1164 | 12 | 44 | 5.06 | 11 | 33 | 7.1 | 356. | 92. | 1366. | -1.0 |
| 1166 | 12 | 44 | 7.85 | 11 | 31 | 54.9 | 415. | 33. | 1126. | -1.0 |
| 2001 | 12 | 43 | 36.72 | 11 | 30 | 22.7 | -3. | -174. | 1391. | -1.0 |
| 2002 | 12 | 43 | 37.68 | 11 | 30 | 11.5 | 13. | -181. | 1648. | -1.0 |
| 2003 | 12 | 43 | 38.16 | 11 | 30 | 38.2 | 13. | -154. | 971. | -1.0 |
| 2004 | 12 | 43 | 38.16 | 11 | 30 | 45.7 | 11. | -146. | 1024. | -1.0 |
| 2007 | 12 | 43 | 39.12 | 11 | 32 | 7.8 | 4. | -63. | 1045. | -1.0 |
| 2029 | 12 | 43 | 42.48 | 11 | 32 | 16.1 | 49. | -43. | 860. | -1.0 |
| 2041 | 12 | 43 | 45.12 | 11 | 32 | 33.4 | 82. | -16. | 1392. | -1.0 |
| 2042 | 12 | 43 | 45.36 | 11 | 31 | 0.5 | 110. | -105. | 845. | -1.0 |

Notes. The x, G and y, G coordinates are in arcsec, measured from the center of M 60. Their orientation is described in the text. A value of -1 for $m(5007)$ indicates that it was not measured.

Table 4. PN Candidates more likely to belong to NGC 4647

| ID | α (J2000) | | | δ (J2000) | | | x , G | y , G | Helioc. RV (km s ⁻¹) | m (5007) |
|------|---------------------|----|-------|---------------------|----|------|---------|---------|-------------------------------------|---------------|
| 1029 | 12 | 43 | 30.14 | 11 | 32 | 37.6 | -131.6 | -68.8 | 1419.4 | -1.0 |
| 1050 | 12 | 43 | 32.43 | 11 | 33 | 21.4 | -110.4 | -17.8 | 1477.7 | -1.0 |
| 3 | 12 | 43 | 33.09 | 11 | 35 | 51.3 | -139.8 | 129.5 | 1433.5 | 27.3 |
| 4 | 12 | 43 | 34.03 | 11 | 35 | 40.3 | -123.7 | 122.5 | 1463.0 | 27.6 |
| 6 | 12 | 43 | 34.73 | 11 | 35 | 42.4 | -114.3 | 127.2 | 1415.2 | 26.8 |
| 9 | 12 | 43 | 35.16 | 11 | 35 | 56.4 | -111.8 | 142.3 | 1424.1 | 26.6 |
| 11 | 12 | 43 | 35.28 | 11 | 34 | 9.9 | -82.5 | 39.9 | 1479.6 | 26.9 |
| 14 | 12 | 43 | 35.88 | 11 | 34 | 8.7 | -73.7 | 41.0 | 1480.8 | 26.6 |
| 17 | 12 | 43 | 36.22 | 11 | 34 | 29.7 | -74.3 | 62.6 | 1437.8 | 27.3 |
| 21 | 12 | 43 | 36.46 | 11 | 34 | 58.1 | -78.3 | 90.9 | 1471.1 | 27.0 |
| 22 | 12 | 43 | 36.79 | 11 | 34 | 58.5 | -73.6 | 92.6 | 1448.2 | 26.8 |
| 24 | 12 | 43 | 37.01 | 11 | 36 | 0.2 | -86.5 | 153.0 | 1423.1 | 27.0 |
| 25 | 12 | 43 | 37.20 | 11 | 33 | 52.5 | -50.7 | 30.4 | 1444.0 | 26.8 |
| 27 | 12 | 43 | 37.61 | 11 | 35 | 18.4 | -67.2 | 114.9 | 1464.0 | 27.1 |
| 31 | 12 | 43 | 38.06 | 11 | 35 | 42.4 | -67.0 | 139.8 | 1498.5 | 27.7 |
| 33 | 12 | 43 | 38.16 | 11 | 35 | 1.1 | -54.9 | 100.3 | 1406.8 | 26.6 |
| 34 | 12 | 43 | 38.38 | 11 | 35 | 1.4 | -51.8 | 101.4 | 1465.2 | 27.0 |
| 37 | 12 | 43 | 38.66 | 11 | 34 | 39.4 | -42.2 | 81.2 | 1447.5 | 27.5 |
| 39 | 12 | 43 | 38.76 | 11 | 35 | 48.7 | -58.7 | 148.6 | 1478.4 | 27.3 |
| 47 | 12 | 43 | 39.24 | 11 | 34 | 32.7 | -32.2 | 77.0 | 1445.3 | 27.1 |
| 50 | 12 | 43 | 39.36 | 11 | 35 | 43.8 | -48.9 | 146.1 | 1433.2 | 27.2 |
| 54 | 12 | 43 | 39.46 | 11 | 34 | 36.8 | -30.2 | 81.8 | 1407.3 | 27.8 |
| 60 | 12 | 43 | 39.70 | 11 | 35 | 9.2 | -35.1 | 114.0 | 1431.7 | 27.0 |
| 62 | 12 | 43 | 39.74 | 11 | 35 | 2.0 | -32.7 | 107.2 | 1433.0 | 26.5 |

Table 4—Continued

| ID | α (J2000) | | | δ (J2000) | | | x , G | y , G | Helioc. RV (km s ⁻¹) | m (5007) |
|-----|---------------------|----|-------|---------------------|----|------|---------|---------|-------------------------------------|---------------|
| 72 | 12 | 43 | 40.29 | 11 | 34 | 5.8 | -10.3 | 55.0 | 1438.0 | 27.1 |
| 99 | 12 | 43 | 41.62 | 11 | 35 | 22.8 | -11.4 | 134.4 | 1451.4 | 27.2 |
| 109 | 12 | 43 | 41.98 | 11 | 36 | 1.4 | -16.3 | 173.1 | 1440.1 | 27.1 |
| 120 | 12 | 43 | 42.48 | 11 | 34 | 46.2 | 10.3 | 102.4 | 1448.7 | 26.4 |

Notes. The x, G and y, G coordinates are in arcsec, measured from the center of M 60. Their orientation is described in the text. A value of -1 for $m(5007)$ indicates that it was not measured.